



Spatiotemporal Correlation Analysis of Jet Noise from a Round-Nozzle Supersonic Aircraft

S. Hales Swift*, Kent L. Gee†, and Tracianne B. Neilsen‡
Brigham Young University, Provo, UT 84602

Alan T. Wall§
Air Force Research Laboratory, Wright-Patterson Air Force Base, OH, 45433

J. Micah Downing¶ and Michael M. James||
Blue Ridge Research and Consulting, Asheville, NC, 28801

Spatiotemporal analysis of noise from a tethered F-35B provides insight into the spatial, spectral and temporal relationships within the sound field. Six engine power conditions ranging from 25% to 150% engine thrust request were measured using a 71-microphone linear ground array located approximately 8 m from the estimated shear layer. Mixing noise trends with engine power for the round-nozzle F-35B are similar to those of a nominally rectangular-nozzle high-performance jet aircraft [Harker et al, AIAA, 2016]. Cross-correlation and coherence measures are used to corroborate and confirm identifications of fine- and large-scale turbulent mixing noise contributions from a concurrent study of the F-35B dataset [Neilsen et al., AIAA, 2018].

The relationships observed between multiple spatio-spectral lobes seen in the maximum radiation regions of prior and concurrent high-performance aircraft noise studies [Lee et al., AIAA, 2018] are confirmed and expanded upon. Correlograms help identify how the multiple spatio-spectral lobes have different apparent phase speeds across the array, corresponding to different directionality, some components of which also change with engine power. Increased overlap of lobes with increased engine power appears to drive global decreases in field coherence. Finally, the structure of the spatio-spectral lobes appears to be more visible in nondimensionalized coherence length than in the spectrum itself.

Broadband shock-associated noise (BBSAN) is found in the upstream direction at engine powers of 75% engine thrust request and above. Coherence is also used to separate BBSAN from jet mixing noise because the BBSAN is coherent within the relevant frequency range while adjacent fine-scale mixing noise is not. However, correlation and coherence analyses show that the upstream BBSAN signature is related to sound received in the peak radiation region dominated by the spatio-spectral lobes. Possible links between the shock-associated noise and the spatio-spectral lobes are discussed.

Nomenclature

(Nomenclature entries should have the units identified)

A^2	=	correlation envelope
BBSAN	=	broadband shock-associated noise
c	=	speed of sound
c_{eff}	=	propagation speed in the direction of the line array
dB	=	sound pressure level in decibels referenced to 20 micropascals (μPa) or referenced to $20\mu\text{Pa}/\sqrt{\text{Hz}}$

*Postdoctoral Fellow, Department of Physics and Astronomy, N233 ESC, and AIAA Member.

†Professor, Dept. of Physics and Astronomy, N243 ESC, and AIAA Senior Member.

‡Associate Professor, Dept. of Physics and Astronomy, N251 ESC, and AIAA Member.

§Research Physicist, Battlespace Acoustics Branch, 2610 Seventh St., Bldg. 441, AIAA Member.

¶President and Chief Scientist, 29 N Market St, Suite 700, AIAA Member.

||Sr. Vice President and Chief Engineer, 29 N Market St, Suite 700, AIAA Member.

ETR	=	engine thrust request, the main engine power setting descriptor
f	=	frequency
FS	=	fine-scale turbulence noise
FSS	=	fine-scale turbulence noise spectral shape
G_{xy}	=	one-sided cross-spectrum of x and y
G_{xx}	=	one-sided auto-spectrum of x
L_{γ^2}	=	coherence length
LS	=	large-scale turbulence structure noise
LSS	=	large-scale turbulence structure noise spectral shape
MARP	=	microphone array reference point
OASPL	=	overall sound pressure level referenced to 20 micropascals
$\hat{r}_{x,y}$	=	cross-correlation coefficient of x and y
$\hat{R}_{x,y}$	=	unnormalized cross-correlation of x and y
SPL	=	sound pressure level referenced to 20 micropascals
z	=	distance downstream from the nozzle
γ^2	=	coherence
λ	=	wavelength

I. Introduction

SPATIO-TEMPORAL-SPECTRAL analyses provide insight into the properties and dynamics of a sound field imprinted with the unique characteristics of the underlying production mechanisms. For example, Tam *et al.* [1] analyzed spectra, coherence and cross-correlation of the sound field, and correlation between jet flow measurements and the far-field noise from a laboratory-scale jet, and applied an acoustic mirror technique to establish the highly productive two-source model of jet mixing noise first suggested by Schlinker [2]. Nance [3] similarly employed multi-microphone correlation and coherence to discriminate between large-scale turbulent structure noise, fine-scale turbulence noise and core noise contributions in the near-field of a laboratory-scale jet. The noise generated by large-scale turbulent structures and fine-scale turbulence differs markedly in coherence and correlation properties making these tools valuable for identifying and studying regions of the sound field affected by these jet mixing noise sources.

Evaluating correlations between flow variables and the acoustic field of laboratory-scale jets has also enabled researchers to better understand the relationships between the flow and acoustic fields. Panda *et al.* [4] were able to link turbulent flow quantities to the received sound field by examining correlation between velocity and density measurements at points in the plume of a jet using an optical system and the far-field sound. By doing this they were able to glean insights into the relative significance of various flow quantities for acoustic production. Papamoschou *et al.* [5] evaluated the correlation between optical deflectometry probes and far-field noise measurements, finding a significant correlation between the output of probes located in the jet shear layer and the far-field noise in the peak radiation direction and providing empirical evidence for the importance of large-scale turbulent structures in noise radiation from jets. Liu *et al.* [6] investigated correlations between near-field acoustic pressure and jet turbulence quantities in large-eddy simulations of jets with and without shock cells and the associated noise production mechanisms. These correlations yielded insights into differences between the acoustic radiation of upstream and downstream noise source regions, as well as other aspects of the structure of sound production within a simulated military-style jet.

The jet noise field can also be used to provide information on some aspects of the flow. Baars and Tinney [7] used correlation between a near-field linear microphone array and a far-field circular microphone array to investigate the convective velocities of heated and unheated laboratory-scale jets and identify mechanisms through which near and far-field pressures are coupled. Correlations between pairs of microphones located within or in proximity to a laboratory-scale jet were examined by Fuchs *et al.* [8]. By comparing changes in correlation with separation in multiple directions for filtered and unfiltered pressure signals, they were able to show significant anisotropy in the turbulence structures within a round jet.

Spatial correlation relationships also contain important information for constructing high-fidelity models of the jet sound field. Kumar *et al.* [9] utilized far-field correlation in studying differences between converging-diverging and aerospoke laboratory-scale nozzles at under, over, and ideally expanded conditions. Maestrello *et al.* [10], mapped two-point correlations in the vicinity of a laboratory-scale jet, noting the value of this correlational information for interpreting and modeling the sound field. Harker used the cross-beamforming as input to a multiple wavepacket-based

approach for modeling the sound field with the objective of capturing both level and coherence properties of the sound field [11].

Acoustic correlation information can also yield insights into source characteristics and locations independent of availability of flow variables. This is especially an important avenue of investigation given the current challenges in obtaining flow data from high-performance, military engines. Fuchs *et al.* [8] suggested the existence of a non-compact jet noise source on the basis of correlational evidence. Fisher *et al.* [12] made use of correlation in a far-field microphone arc to identify the effective source locations of jet engine noise. Viswanathan *et al.* [13] used correlation and coherence analyses of the noise field from perfectly expanded laboratory-scale jets operating under a variety of Mach numbers and were successful in identifying a large coherent source region that had not previously been documented, though Jordan and Colonius [14] noted the possibility of a different interpretation of the observed phenomenon. Schlinker *et al.* [15] investigated the noise emissions of an uninstalled full-scale engine operating at high engine power and used acoustic beamforming in order to determine source distribution seen from the peak radiation direction and to investigate the origin of impulsive events within the jet plume. Harker *et al.* [16] similarly used the DAMAS-C beamforming algorithm to assess source coherence and power and showed important contributions of uncorrelated sources in the dominant source region of their full-scale aircraft.

Spatiotemporal analysis is also increasingly important in characterization and comparative studies of jet noise from engines installed in high-performance military aircraft. Harker *et al.* [16] applied spatiotemporal analysis tools, similar to those of Viswanathan *et al.* [13] for laboratory-scale jets, to the sound field surrounding a single active engine of a modern advanced tactical aircraft, operated at two engine conditions. This study enabled identification of points of commonality and difference between laboratory-scale jet noise and those of a full-scale, tactical aircraft engine noise. A key point of difference was the presence of multiple self-coherent but mutually incoherent spatio-spectral lobes. Although only two lobes were visible in the one-third octave band spectra presented by Harker *et al.* (see Fig. 2 of Harker *et al.*), this effectively opened the door for further analyses of this phenomenon. Harker *et al.* also identified a bifurcated region in the cross-correlogram at afterburner (see Fig. 8 of Harker *et al.*). They rightly noted that this indicated waves traveling with identifiably different phase speeds and far-field directivity but stopped short of calculating the resultant direction of propagation.

The present F-35 study follows in the tradition of Harker *et al.* [16] and Viswanathan *et al.* [13], as well as the acoustical measures in Tam *et al.*'s [1], in using correlation, coherence, and spectra across array locations in order to gain insights into key sound field and source characteristics. In this paper, however, several new analysis methods are introduced that provide additional insights into the structure of the sound field surrounding a high-performance military aircraft and yield information important for modeling jet noise. In this study, a 71 microphone, linear ground array (located approximately 8 m from the estimated shear layer) is used to capture the sound field from the installed Pratt & Whitney F-135 engine operated at six conditions ranging from 25% Engine Thrust Request (ETR) to 150% ETR (maximum afterburner). The detailed analyses enable comparisons both across F-35 engine conditions and between the F-35 and the tactical aircraft study of Harker *et al.* [16]. As well as exploring the manifestations of fine-scale turbulence (FS) noise and large-scale turbulence structure (LS) noise through correlation, coherence and spectra, specific analyses are provided to understand the characteristics of the broadband shock-associated noise (BBSAN) in the forward direction and multiple spatio-spectral lobes in the maximum radiation region.

Broadband shock-associated noise is a significant contributor at upstream array positions in the F-35 sound field and is easily visible in cross-correlograms and peak cross-correlation, which show elevated correlation in the region associated with BBSAN spectral contributions. BBSAN has been explored extensively for laboratory-scale jets (see literature review in Ref. [17] for examples). but was not explored in Harker *et al.*'s [16] study, where BBSAN seems to have been a more modest contributor. In contrast to the FS noise also present, the BBSAN tends to increase both the coherence and coherence lengths at the frequencies and locations where it is present. The correlation and coherence measures also, unexpectedly, each show a connection between the BBSAN in the upstream direction and a downstream region generally associated with LS noise [17]. This connection could be seen as consistent with models of BBSAN that indicate that it should be present in all directions but is typically more easily detectable in the forward direction due to competition from the large-scale turbulence structure noise, which is most prominent in the maximum radiation region [18]. This explanation also seems consistent with reports of BBSAN observed in the aft direction during flight [19, 20], though this differs from our static jet case. The correlation between BBSAN and the noise radiation in the maximum radiation region may also be consistent with the observation of Liu *et al.* [21] that BBSAN made its maximum contribution in the aft direction in their large eddy simulation. If this interpretation is correct, then the spatiotemporal techniques in this paper allow detection (and, potentially, quantification) of BBSAN contributions of a tied down F-35B in portions of the sound field where LS noise prevents direct observation of BBSAN in the autospectrum. It may also be

possible that some other mechanism is conveying the same information to both locations. The large-scale turbulent structures, which both generate the Mach wave radiation and actuate the shocks in order to produce BBSAN, might be a potential mechanism for this effect. Whatever mechanism ultimately explains the phenomenon, correlation and coherence at BBSAN frequencies between upstream and downstream locations (but not between) has been observed in this study.

While FS and LS noise and BBSAN have been observed in many laboratory-scale studies, jet noise spectra with multiple peaks resulting from multiple spatio-spectral lobes appear to emerge only under certain conditions. Multiple families of Mach waves are discussed by Seiner *et al.* [22] as well as by Tam *et al.* [23] following initial observations by Oertel [24–26], though the relationship between these phenomena and the lobe phenomenon remains uncertain. Early examples of multilobe observations for full-scale jets have been published by Greska and Krothapalli [27] and Gee *et al.* [28]. Nevertheless, a complete theory explaining this phenomenon remains elusive. The presence of multiple spatio-spectral lobes is clearly visible in the present coherence and correlation analyses of the F-35 noise field, corroborating the findings of Wall *et al.* [29] based on near-field acoustical holography. However, the coherence and correlation analyses indicate a greater number of lobes than the three clearly shown in Wall *et al.*. In addition, the number of lobes increases with engine power condition up to 100% ETR where it remains relatively constant at about 5-6 distinct lobes. Phenomena related to the presence of multiple lobes are identified in cross-correlograms, where the phase speeds of some sound components across the array is observed to change with engine power condition. The array phase speeds of sound components are used to calculate the direction of propagation for each component. The predicted directivity of these components appear to explain the change in far-field directivity of the F-35 with regard to engine power condition [30]. The present study confirms the results of Harker *et al.* [16] that adjacent spatio-spectral lobes are mutually incoherent at narrowband frequencies where both contribute, leading to reduced coherence at multilobe frequencies. The proliferation of spatio-spectral lobes appears to drive the drop in coherence lengths seen with increasing engine power condition where larger numbers of incoherent lobes increase the complexity of the resultant sound field. This trend is confirmed and clarified in the present study because of the larger number of engine power conditions. Properly capturing field coherence properties associated with multiple spatio-spectral lobes is important for modeling of the sound field, e.g., with equivalent wavepacket sources [11]. This study also notes the nearly harmonic structure of the lobe center frequencies. Wall *et al.* [31] has suggested that aspects of the multiple lobe phenomenon may be linked with shock cell structures, and it is possible that both spacing and frequency characteristics of the spatio-spectral lobe structure are in some way reflective of the spacing and characteristics of the shocks.

II. Measurements

Recordings were made of an tied-down F-35B on a run-up pad located at Edwards Air Force Base, as discussed in James *et al.* [30]. The single, round-nozzle, F-135 engine was cycled from IDLE through six power conditions ranging from 25% engine thrust request (ETR) through 50%, 75% (intermediate power), 100% (military power, MIL), 130% (minimum afterburner, MINAB) and, finally, to 150% ETR (maximum afterburner, MAXAB). The nozzle had a variable diameter around 1 m, and the nozzle centerline height was approximately 2 m. Numerous microphone arrays were used to simultaneously capture the sound field at both near- and far-field locations in order to facilitate characterization of the sound field. Several arc arrays were centered around a microphone array reference point (MARP) 7.5 m downstream of the nozzle where the assumed effective acoustic origin was located. However, this study is focused on a 32.0 m (105.0 feet) line array of 71 equally-spaced, 6.35 mm (1/4") microphones placed on the ground approximately parallel with the shear layer as seen in Fig. 1. The microphones were 0.45 m (± 1 cm) apart and were located from 8.5 m upstream of the expected average peak source location to 23.5 m downstream of this position (2.1 m upstream of the nozzle to m downstream of the nozzle). The simultaneous recording across the array at 204.8 kHz using NI PXI-4498 cards makes possible comparisons of the temporal behavior seen at each microphone. The aperture covered a region from upstream of the engine nozzle to well downstream of the maximum radiation region: good coverage for observing BBSAN and FS and LS noise. The use of a ground-based array eliminated uncertainty caused by ground reflections. The use of an array that was approximately parallel to the jet shear layer minimized risk of unwanted effects from the turbulent pressure fluctuations of the jet hydrodynamic near field at location far downstream of the nozzle exit.

Spectral maps facilitate understanding of the variation in noise radiation captured by the linear array. Figure 2 shows, for each engine condition, the autospectral density and overall sound pressure level (OASPL) at all microphone positions. The horizontal coordinates for each of the subplots is the distance relative to the nozzle exit plane, as shown in Fig. 1. Nondimensionalization of the frequency in terms of Strouhal number was not attempted because the precise nozzle exit diameter and jet conditions are not publicly available. The array aperture was successful in capturing the

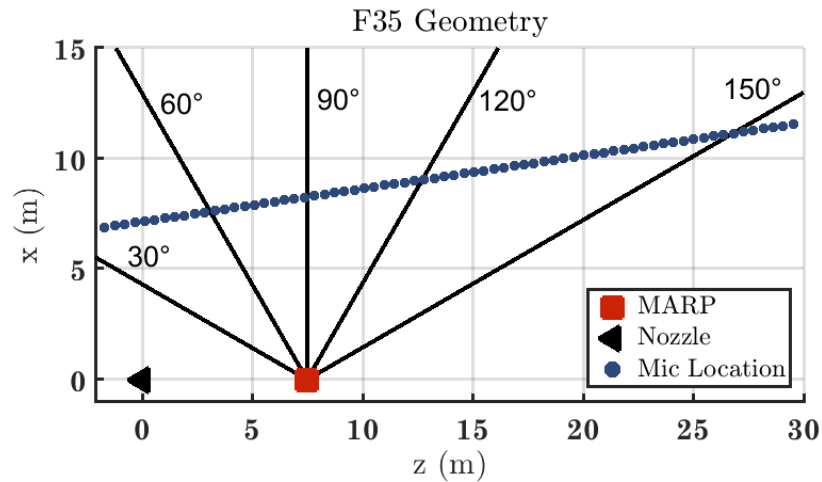


Fig. 1 Setup for the F-35B measurement. The 71 microphone array runs approximately parallel to the assumed shear layer. z is the downstream distance, and x is the sideline distance.

maximum OASPL for each engine condition and, thus, is sufficient for some interesting investigations. Only the top 20 dB of the sound field are shown at each location. This value was chosen because it makes features of interest to this investigation easy to see. These features include the BBSAN signature (visible as a reddish-orange streak in the left quarter of the spatio-spectral plots of 75% ETR and above and discussed further in Sec. IV.C) and the presence of multiple spatio-spectral lobes (visible as between two and six oblong darkened regions easily seen for 50% ETR and above and discussed further in Sec. IV.B). These features, together with jet mixing noise, are discussed in their respective sections so that observation made using a variety of differing techniques can be brought together to develop a coherent picture of each phenomenon.

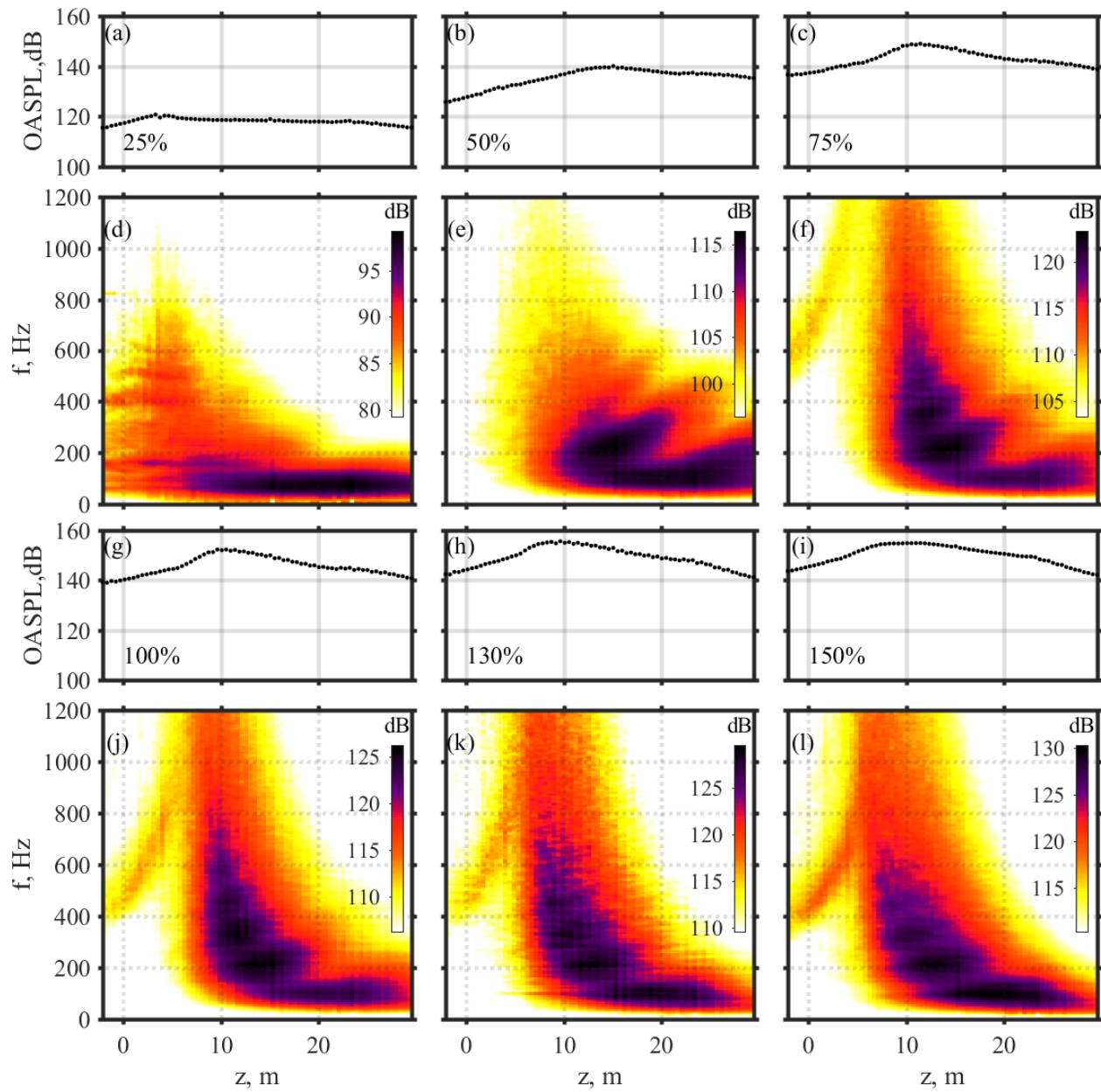


Fig. 2 OASPL (dB) in (a, b, c, g, h, i) and autospectral density levels (dB re $20 \mu\text{Pa}/\sqrt{Hz}$) in (d, e, f, j, k, l) as a function of microphone location for six engine conditions: 25%, 50%, 75%, 100%, 130%, and 150% ETR. Top 20 dB of the autospectral density are shown in each frame.

III. Methods

To clearly describe each of the phenomena investigated in this paper, basic familiarity with the tools of correlation and coherence analyses is required. In order to provide a common basis, each of these methods is briefly described and an example given that should help both exemplify the types of information that each technique provides and illuminate the phenomena under study. The strengths and limitations of each method also receive some attention.

A. Cross Correlation and Coherence

This study also uses the signal processing tools of correlation and coherence. Both correlation and coherence give indications of the relatedness of signals arriving at differing points in the sound field. Correlation as used in this paper is defined in equations 1 and 2. The expected value of the product of two zero-mean signals, s_i and s_j (measured at the i^{th} and j^{th} microphones located at downstream distances of z_i and z_j , respectively) is evaluated as in Eq. 1 for different possible delays, τ , between the two signals

$$\hat{R}_{i,j}(\tau) = E[s_i(t)s_j(t + \tau)]. \quad (1)$$

The correlation, $\hat{R}_{i,j}(\tau)$, is then normalized in one of two ways. The first normalization divides by the square root of the expected values of the two signals multiplied by themselves with 0 delay, i.e., the autocorrelations:

$$\hat{r}_{i,j,coeff}(\tau) = \frac{\hat{R}_{i,j}(\tau)}{\sqrt{\hat{R}_{i,i}(0)\hat{R}_{j,j}(0)}}. \quad (2)$$

The resulting, $\hat{r}_{i,j,coeff}(\tau)$, are essentially correlation coefficients, with values limited to $-1 \leq r(\tau) \leq 1$. The correlation coefficients indicate the similarity of the signals s_i and s_j at a given delay τ . The correlation coefficients were calculated in MATLAB using the “xcorr” function with the “coeff” option for normalization. The second normalization uses the maximum value in the reference channel i as the normalization

$$\hat{r}_{i,j,norm}(\tau) = \frac{\hat{R}_{i,j}(\tau)}{\hat{R}_{i,i}(0)}. \quad (3)$$

This second normalization allows for the preservation of the relative magnitude of signals across the array. This is advantageous when analyzing a sound field with multiple noise components some of which are coherent and present similarly across a large spatial extent and others of which are spatially incoherent. Using this latter normalization, the relative magnitude of components which are correlated with the reference channel can be more easily observed and studied across channels because uncorrelated components are not able to attenuate the signal by increasing the magnitude of the normalizing autocorrelation in the non-reference channel as would be the case if the normalization of Eq. 2 were used. Noise in the non-reference channel is thus prevented from hiding the relationship to the signal. The second normalization is thus used to track signal arrival times across the array, which enables determination of component phase speeds from the trajectories of the correlative streaks and, consequently, the direction of propagation of tracked components.

Often, a logarithmic scaling for the correlation is needed to detect low-level features. As the log of a negative number is undefined, a correlation envelope is defined calculated via the Hilbert transform (denoted by a tilde above the affected variable).

$$A_{i,j} = [r_{i,j,norm}^2 + \tilde{r}_{i,j,norm}^2]^{1/2}. \quad (4)$$

The resultant values of $A_{i,j}(\tau)$ is useful for working with signals containing noise components at a wide variety of levels moving at differing phase speeds relative to the array.

The mathematical expression for coherence is similar to correlation in both form and meaning. Coherence, γ_{ij}^2 , is calculated from the autospectra, $G_{i,i}$ and $G_{j,j}$, and the cross-spectrum, $G_{i,j}$, using

$$\gamma_{ij}^2(f) = \frac{|G_{ij}(f)|^2}{G_{ii}(f)G_{jj}(f)}. \quad (5)$$

For coherence, values are specifically limited to $0 \leq \gamma_{ij}^2(f) \leq 1$. Rather than telling how similar two signals are as a function of time delay, the coherence indicates how similar two signals are in the information they contain at a particular frequency f . Thus $\gamma_{ij}^2(f)$ can be interpreted as the portion of signal power at a given frequency in which two signals

share common information [32]. Because both correlation envelope, A , and coherence, γ^2 , are positive variables proportional to pressure squared, their values in decibels are calculated via $10 \log_{10} A$ and $10 \log_{10} \gamma^2$, respectively, with a reference of one in both cases. A similar procedure was used for the correlation envelope by Harker *et al.* [33].

The significance of coherence and correlation analyses can be further explained by examining the differences across the microphone arrays. In Fig. 3, the correlation (part a) and the coherence (part b) are evaluated for four positions within the microphone array: $z = -2.1, 7.8, 13.3$, and 29.1 m. These positions include the farthest upstream location where BBSAN has its largest contribution, one to the side of the MARP where FS noise is known to be the dominant source, one in the maximum radiation region where LS dominates, and the second farthest downstream microphone location. Each microphone signal i is compared to that of its downstream nearest neighbor j . Consequently, the delay, τ , for the peak in the correlation is positive for microphone pairs that are receiving sound from sources upstream of their position (perpendicular to the array) and negative for those receiving sound from downstream. Thus, the correlation results can be used to deduce relationships within the sound field and apparent acoustic source locations.

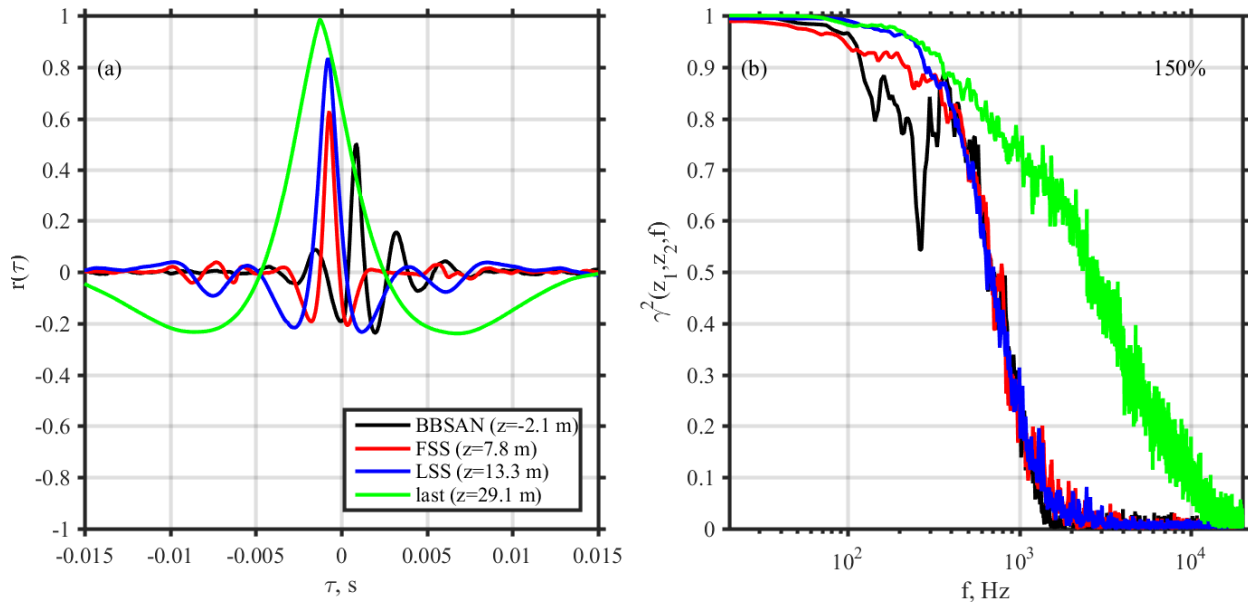


Fig. 3 (a) Cross-correlation and (b) coherence of signals (at 150% ETR) received from microphones at $z = -2.127.83, 13.26$ and 29.08 m with their downstream nearest neighbor in the microphone array.

The spatial variation in the sound field characteristics are evident in the cross-correlation. At the farthest upstream microphone location ($z = -2.1$ m), considerable ringing is seen in the cross-correlation (Fig. 3(a)) associated with the peaked spectral character of the BBSAN. In the FS-dominated region ($z = 7.8$ m), the cross-correlation decays quickly, while in the LS-dominated regions ($z = 13.3$ m) significant correlation persists for longer time delays. The cross-correlation function at the far downstream location ($z = 29.1$ m) appears to differ, likely because the peak frequency of the noise is significantly lower, as seen in Fig. 2.

Similar features are evident in the spatial variation of the coherence. In Fig. 3(b), the narrowband character of the BBSAN is apparent as a peak in the coherence between 250-700 Hz. The FS-dominated position dips in coherence earlier than the others, but follows a similar general pattern in decay to all but the farthest aft location.

The observed elevation of the coherence at lower frequencies appears to reflect the significance of wavelength in calculations of coherence. Microphones that are compared at a frequency for which they are separated by a small fraction of a wavelength tend to exhibit high coherence because of the large quantity of information which they share. Thus, for fixed microphone locations, lower frequencies exhibit greater coherence. The downstream position exhibits a higher degree of coherence at higher frequencies in part because the microphones at the end of the array cover a relatively smaller angular aperture and the sound field is propagating closer to parallel with the array at this point. Thus these microphones share more information in common between them because of the near-parallel direction of propagation.

Correlation-based considerations play an important role in the coherence calculation. To calculate coherence values reflective of the real relationships that exist between signals across a long array of microphones, signals related to one

another must be analyzed within the same block of the discrete Fourier transforms, which are an important intermediate step in calculating the coherence calculation. This alignment can be accomplished by using processing block lengths much longer than the propagation delay between microphones, or the signals must be delayed (time-aligned) prior to the discrete Fourier transforms. For the coherence calculations in this paper, the block length is long relative to typical signal delay times between microphones. Analysis of correlograms (tau-dependent cross-correlation coefficients for each microphone pair) confirm that typical delays across our array were on the order of 0.06 s. The block length was chosen to be 32768 samples long; at a sampling frequency of 204,800 Hz, the block length was thus 0.16 seconds for all coherence calculations. Second, in this paper delay values were determined from analyzing correlative peaks between multiple reference microphone positions and the entire array. These delay values were used to time-align the signals used in coherence calculations so that shared information arrives roughly simultaneously, thus, ensuring that coherent relationships between signals from different positions within the field are correctly assessed. By using large block sizes and appropriately delaying the signals, the approach taken in this paper seeks to calculate the maximum coherence at each frequency.

B. Correlation and Coherence 3-Dimensional Matrices

Once correlation and coherence are successfully calculated, it is worthwhile to consider how to compare values across a linear array of sensors. Both correlation and coherence can be calculated between all pair of microphones, and can, thus, contain three dimensions—two dimensions of position or microphone number (i, j) and one dimensions of delay τ (for correlation) or frequency (for coherence). This is depicted graphically in figure 4 for the resulting correlation, correlation envelope and coherence matrices.

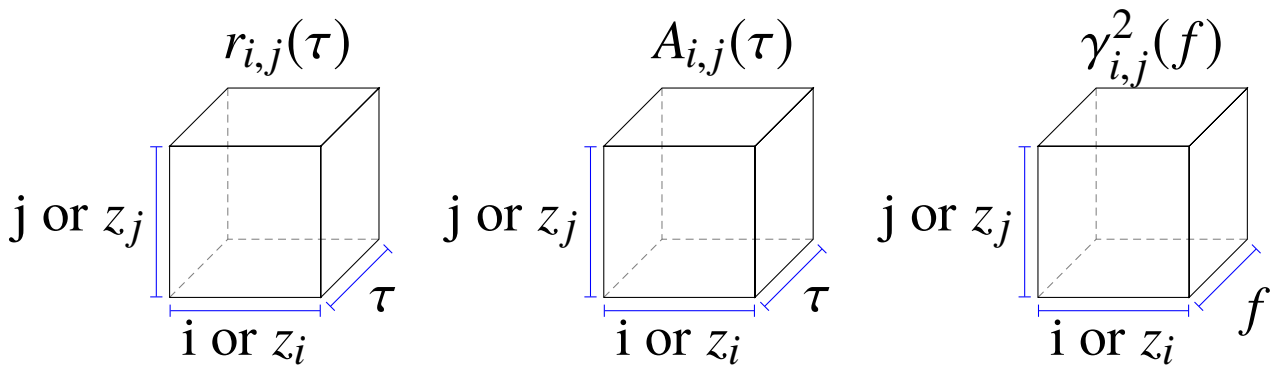


Fig. 4 Depiction of correlation r , correlation envelope A (absolute value of Hilbert transform of correlation) and coherence γ matrices for a linear microphone array. The correlation and correlation envelope have independent variables of delay τ and the positions of the two microphones while coherence has the independent variables of frequency f and the positions of the two microphones.

While a 3-dimensional matrix can fully capture the relationships that exist within the sound field, the usefulness of this approach is limited by the ability to visualize and, thus, interpret and understand data in such a format. Instead, different methods are needed to more easily visualized summary measure of correlation or coherence; typically information about correlation and coherence can be gleaned from a slice or contraction of the 3-dimensional matrix.

C. Single-Reference Cross-Correlation and Coherence and Single-Frequency Array Coherence

One type of slice of the correlation and coherence information is based on the selection of a single reference microphone. By selecting a single value for i (the reference microphone number), all of the cross-correlations or coherence of microphone i with the entire array may be viewed simultaneously. Single-reference correlation, also called a correlogram, is most useful for determining directions of propagation of broadband components based on their phase speed along the array. Single-reference coherence shows the relationship between the information received at a particular point along the microphone array and the information received across the entire array as a function of both location and frequency.

Examples of single-reference correlation and coherence maps are shown for demonstration purposes in Fig. 5. The single-reference correlation envelopes (Eq. 4, expressed in decibels) are displayed for the first, middle, and last

microphones in the array (located at $z = -2.1, 13.7$ and 29.5 m) in parts (a), (b) and (c) of the figure. The single-reference coherence is shown (also in decibels) at the same three locations in parts (d), (e) and (f), respectively. Downstream location, z , is the horizontal axis for all the plots. The vertical axis is time delay τ for the correlation plots and frequency f for coherence plots, and non-negativity has been exploited in order to use of a common decibel color scale for all plots.

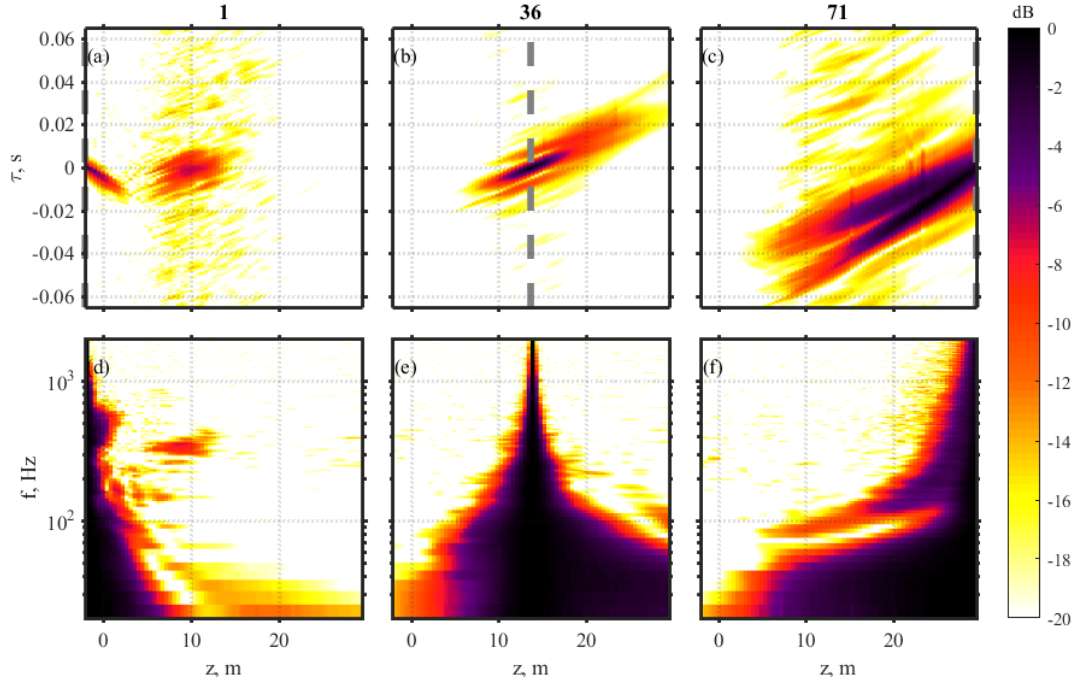


Fig. 5 (a, b, c) Correlation envelope A (in decibels, with normalization in Eq. 3) and (d, e, f) coherence (also in decibels) of a single reference microphone with all array microphones. Examples are displayed for the 150% ETR and three reference microphones, located at $z = -2.1, 13.7$ and 29.5 m, as indicated by gray dashed lines on the upper plots.

Instead of choosing a slice of the coherence matrix based on the position of microphone i , the spatial variation in coherence at a single frequency can be viewed. The resulting slice shows the coherence of all microphone pairs with one another at a particular frequency. An example of this slice is shown in Fig. 6, with $f = 25$ Hz chosen to be well below the ranges where BBSAN and multilobe coherence behaviors might serve as confounders. In this figure, the narrowband autospectral density is plotted above the array coherence. The coherence of the sound field at 25 Hz suddenly changes at $z \approx 14$ m and becomes more coherent across greater microphone separation distances, likely due to the increased coherence of the LS noise over the FS noise. The right part of the figure shows the same relationships as a function of angle, which helps clarify the position and degree of increase in coherence present at downstream locations in the sound field. Comparing the two parts of the figure also shows the potential role of the array geometry in exhibiting greater apparent relationships toward ends which cover a smaller angular range than at some intermediate portions of the array.

D. Peak Cross-Correlation

A slice across the coherence matrix at a single frequency yields useful information (Fig. fig:ArrayCoherence25), but an analogous slice in correlation for a specific time delay τ is less informative due to the arrival of multiple signal components across the array with modestly differing delays. Instead, it is more useful to evaluate the maximum or peak cross-correlation over all delays for each pair of signals. The resulting peak cross-correlation map then yields a measure of broadband relatedness of signals at differing points within the field. Peak cross-correlation coefficients are discussed in Sec. IV.A, Fig. 8, where coefficient values are shown for all engine conditions.

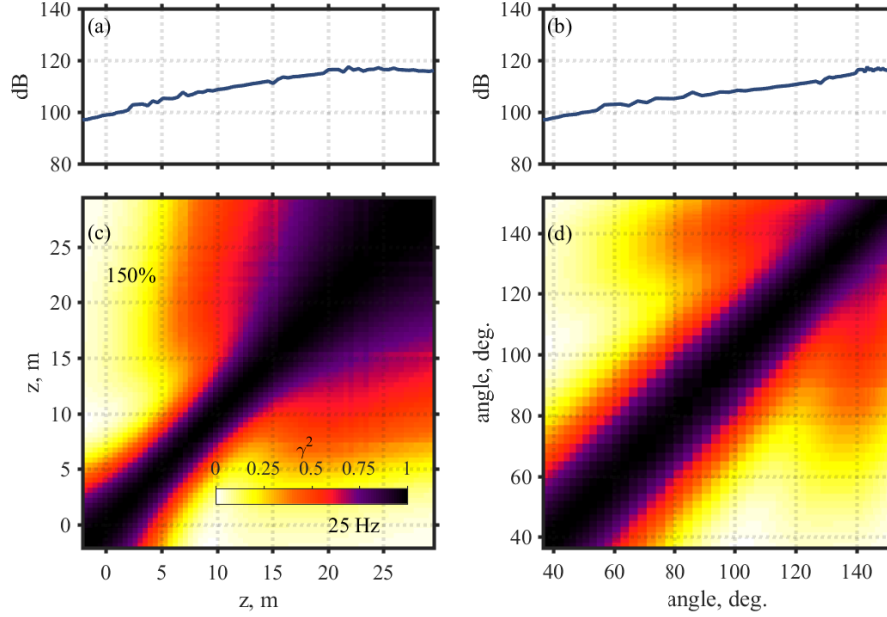


Fig. 6 (a,b) Narrowband autospectral density levels (dB re $20 \mu\text{Pa}/\sqrt{\text{Hz}}$) and (c,d) coherence at 25 Hz across all microphone pairs, plotted as a function of linear position along the array, in (a) and (c), and as a function of angle with respect to the MARP, in (b) and (d).

E. Coherence Length

Because it is not straightforward to summarize relationships contained in the 3-dimensional coherence matrix across frequencies and between multiple positions simultaneously, coherence length is a useful measure to view the spatio-spectral variation in coherence. The upstream coherence length at a particular position, z_i , and frequency, f , is the greatest distance, L , from z_i on the array such that the coherence between the point at z_i and the upstream point at $z_j = z_i - L$ is 0.5:

$$L_{\gamma^2}(z, f)^{\text{up}} = \max \{L\} : \gamma^2(z, z - L, f) = 0.5. \quad (6)$$

A coherence value $\gamma^2 = 0.5$ indicates that half of the information at a given frequency is common between two signals or if two sources (one of which is the reference) are equal contributors at a given frequency. Thus, the upstream coherence length, $L_{\gamma^2}(z, f)^{\text{up}}$, is the maximum distance upstream where half of the signal at frequency f is shared between z_i and z_j . The threshold of $\gamma^2 = 0.5$ was also used previously in the full-scale jet study of Harker *et al.* [16] and so allows for a degree of continuity between studies.

One problem with expressing a summary coherence relation as a dimensional length is that it ignores how wavelength varies with frequency. If the coherence between a pair of signals recorded from an array at two frequencies is evaluated then, all other factors being equal (i.e., the sound field being equally coherent at all frequencies), the sound with the lower frequency has the greater coherence length because its wavelength is longer. This suggests that there may be some utility in evaluating the coherence length as nondimensionalized by the wavelength. This scaling, i.e.,

$$L_{\gamma^2}(z, f)/\lambda(f), \quad (7)$$

is used for some analyses (e.g., Fig. 15, where Eq. 7 is used), but other analyses are presented without nondimensionalization (e.g., Fig. 10 using Eq. 6) for the purpose of maintaining continuity with prior research.

This coherence length nondimensionalization procedure is limited by the spacing of the microphone array. For frequencies where the wavelength is shorter than the inter-microphone spacing, the accuracy may be limited in regions and at frequencies with lower coherence. For this microphone array, the spacing employed was 0.45 m or 1.5 ft. A 0.45 m wavelength is associated with a frequency of $f = 762$ Hz. Above this frequency, it may be difficult to resolve coherence lengths of less than a wavelength and the values may be artificially inflated, although the angle with which the sound approaches the array also plays an important role. Additionally, the small angular difference between microphones at the far aft end of the array may also lead to artificially inflated values at these positions, a form of end-fire effect.

1. Local coherence

A second means of displaying a summary measure of coherence is also considered in this work that is referred to as local coherence. To quantify the local coherence across the microphone array, coherence is calculated between each microphone and a microphone a fixed number of wavelengths (i.e., a fixed, nondimensional distance) downstream,

$$\gamma^2(z, z + 0.7\lambda(f), f). \quad (8)$$

The local coherence analysis can be thought of as a sort of “smart slice” of the coherence 3-dimensional matrix. This slice eliminates the stray length scale of distance between points through nondimensionalization and consequently enables a relatively simple summary assessment of the local field coherence across frequency. In this study, the separation distance of 0.7λ was chosen because, after trying a variety of values, it enabled relatively good contrast between regions dominated by LS and FS noise. The resultant local coherence, with its more equal treatment of differing wavelengths—longer wavelengths typically enjoy longer coherence lengths because of their longer wavelength if this is not accounted for—more effectively distinguishes between noise sources with differing coherence properties, such as LS and FS noise and BBSAN contributions. The limitations described above concerning end-fire effects and frequency limitations due to array spacing also apply here. Notwithstanding these limitations, the use of a nondimensionalized downstream distance to define local coherence has made possible a more physically meaningful analysis of coherence than is possible using measures that neglect to account for the role of wavelength in the behavior of coherence between distant points. This technique is used particularly in Sec. IV.A.

IV. Analysis

A. Mixing Noise

1. Spectra

Schlinker originated the idea that two sources were present in jet mixing noise [2]. Tam *et al.* [34] later developed spectral profiles (similarity spectra) corresponding to the two prominent mixing noise sources: noise generated by large-scale turbulence structures (LS) and noise generated by fine-scale turbulence (FS). Strong evidentiary support for this model as it pertains to laboratory-scale jets was assembled by Tam *et al.* [1]. As part of their study, they showed that the fine-scale and large-scale similarity spectra (referred to hereafter as the FSS and LSS spectrum, respectively) could be used to fit measured data from laboratory-scale jets. Neilsen *et al.* [35, 36] applied the Tam similarity spectra paradigm to noise from a single, installed, rectangular nozzle engine of a full-scale, high-performance jet aircraft. They found that combinations of the FSS and LSS spectral profiles provided a good fit to the measured spectra except at high frequencies (where they believed nonlinearity had affected the spectral slopes), in regimes where a spectral double peak occurred.

Neilsen *et al.* [17] also performed a spectral decomposition of the F-35 data under consideration in this paper. In their study, three spectral profiles, the LSS and FSS spectra of Tam and the BBSAN spectral shape Kuo [19, 20] produced as a simplification of Tam’s earlier model [37, 38], were fit to the spectra at each of the 71 microphone locations along the line array. Theirs is the first detailed study of an installed full-scale jet to include BBSAN in a spectral decomposition of the sound field. This allows a more accurate representation of the spectral contributions of each source to the total sound field because it reduces the potential for misattribution errors. Several principles were followed in their fitting procedure:

- 1) Best fit in the peak-frequency region
- 2) Maintaining smoothly varying OASPL and peak frequency for each of the three components
- 3) Choosing only a single peak frequency for the FSS spectral component, which is consistent with the suggestion of Morris that the peak frequency of the FSS component “varies only slightly” [39].

Based on this procedure they determined levels and peak frequencies for each of the three components when identifiably present. Their paper may be examined for further details as to context, process and results. However, we have replotted their data classifying each microphone position in terms of which of the three components made a spectrally identifiable contribution. These are shown in Fig. 7 for 75% and 150% ETR.

The F-35B spectral decompositions are similar to findings for laboratory jets [34] and a rectangular-nozzle full-scale jet [35]. FS contribution are usually noted forward and to the side sideline of the expected peak source location (marked with a +), and LS noise is the dominant contribution farther aft. In between these regions a combination of LS and FS noise agrees with the radiated spectral shapes. For the F-35B, the FS noise only region is very narrow for 75% ETR and

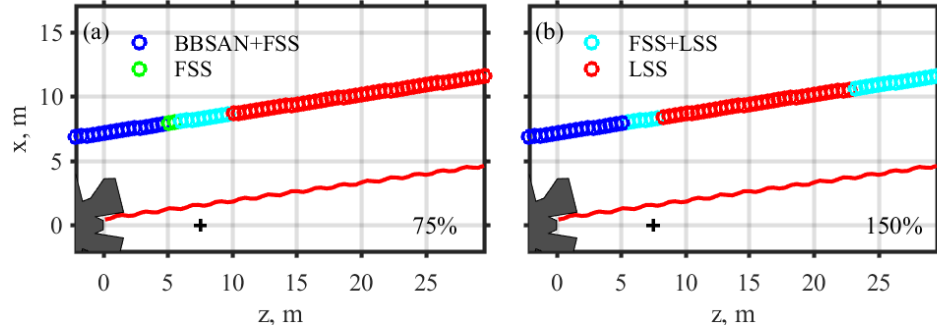


Fig. 7 Schematic of identifiable noise sources across the line array as determined in the spectral analysis of Neilsen *et al.* [17] for two engine conditions: a) 75% ETR and b) 150% ETR. The assumed peak source location is marked as a +, the nozzle is marked using a triangle, and the approximate shear layer is represented as a wavy red line.

nonidentifiable for 150% ETR because of the presence of BBSAN in the forward direction. Differing from previous spectral decompositions which neglected this component, Neilsen *et al.*'s [17] analysis identifies a region where BBSAN makes a prominent spectral contribution on top of the FS noise. At 150% ETR, the LS noise-dominated region shifts slightly forward with the increased engine power condition, consistent with the expected change in directivity of LS noise for an increase in jet convective Mach number. Neilsen *et al.* also identify FS spectral components for locations farthest downstream at 150% ETR, but the LSS spectra dominates at the frequencies analyzed in this paper.

2. Correlation and coherence

Various studies have linked correlation and coherence analyses to mixing noise characteristics. The evidence which Tam *et al.* [1] used in establishing the two-source model of jet mixing noise included not only analysis of spectra, but also coherence and cross-correlation of the sound field, correlation between jet flow measurements and the far field, and use of an elliptical acoustic mirror in order to investigate noise source characteristics. Correlation and coherence between microphones were found to assume lesser values in the FS-dominated region and greater values in the LS-dominated region. Viswanathan [40] showed links between the two jet mixing noise spectra and the correlation of the field at locations dominated by each. When the far-field spectral measurements matched the FSS spectral shape, the correlation was minimal. On the other hand, when the far-field spectra matched the LSS spectral shape the correlation was greater. Nance [3] similarly employed multi-microphone correlation and coherence to discriminate between LS noise, FS noise and core noise contributions in the near-field sound of a jet. The LS and FS noise components differs markedly in coherence (and correlation) properties making these tools valuable for identifying and studying regions of the sound field affected by these jet mixing noise sources. We follow their line of investigation by exploring the correlation and coherence of the sound field in light of the identifications made by Neilsen *et al.* [17]. First, the peak cross-correlation coefficients between microphone pairs is examined followed by two summary measures of field coherence: local coherence and nondimensionalized coherence length.

The peak, pairwise, cross-correlation coefficients shown in Fig. 8 reflect the presence of FS and LS noise sources for the F-35B for six engine powers, as well as elucidating other interesting trends. One noticeable feature of these plots is the growth in correlation over greater distances at locations farther downstream. The previously noted potential end-fire effects caused by angling the array to be nominally parallel to the shear layer could partially contribute to this increase in peak correlation coefficient. However, the results are qualitatively similar to those of Harker *et al.* [16], where the array was parallel to the jet centerline and end-fire effects would have been less prominent. Thus, insights into the mixing noise characteristics can be obtained.

The results in Fig. 8 show evidence of both FS and LS noise. The influence of the FS noise source can be seen best at conditions of 50% and above as a significant contraction or neck in the correlation pattern centering around $z = 3 - 5$ m. At locations farther downstream, the LS noise with its coherent turbulence production mechanism, leads to high levels of correlation between more distant points on the array. However, a trend toward decreasing correlations over comparable distances with increased engine power is visible, suggesting that the field is becoming increasingly incoherent as engine power increases. This may be viewed as unexpected because prior laboratory-scale analyses

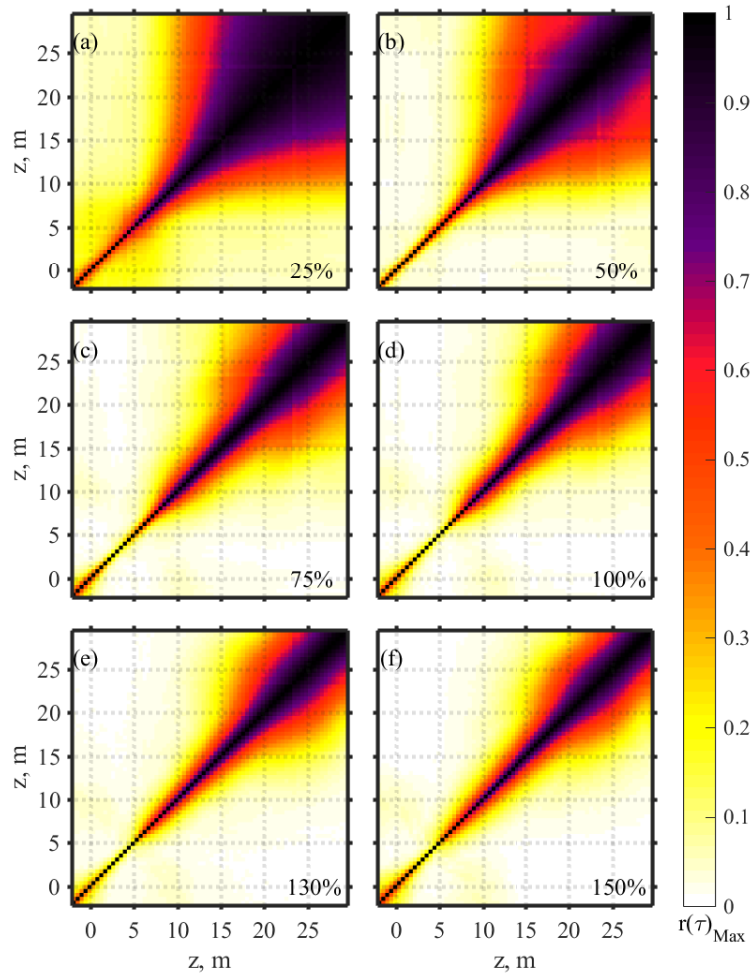


Fig. 8 Peak cross-correlation coefficients for all microphone pairs as a function of downstream distance relative to the nozzle. All six engine conditions are shown.

indicate a greater presence of LS noise with increasing Mach number. That the F-35B peak correlation maps reflect the opposite trend with engine power thus seems notable. This observation is investigated further with coherence analyses.

One additional comment regarding Fig. 8 is worthwhile. For engine conditions of 75% and above, elevated peak correlation coefficients (0.05) are seen between signals from array positions around $z = 0$ and $z = 10$ m downstream. This additional region of correlation, which has not been noted in prior studies, suggests a correlation between noise located at upstream positions associated with BBSAN and downstream positions associated with the maximum radiation region associated with LS noise and the multilobe phenomenon. This correlation is discussed further in Sec. IV.C.

3. Local coherence

As discussed in Sec. III.E, summary measures of coherence need to account for the stray length scale (i.e., the distance) connecting the two positions at which the coherence is to be evaluated. To account for this, the local coherence is calculated with a downstream look distance of 0.7λ as defined in Eq. 8 for 75% and 150% ETR. The top portion of Fig. 9 shows the same spectral classification schematic with results from Neilsen *et al.* [17] shown previously with results for (a) 75% and (b) 150% ETR. The bottom portion of Fig. 9 shows the local coherence for (c) 75% ETR and (d) 150% ETR. Plotting the classification and the local coherence with the same horizontal axis simplifies comparison of results. Interpolation of the coherence results is used when the specified length ($z_i + 0.7\lambda$) falls between microphone locations, but extrapolation is not employed at the downstream end of the array, leading to a blank portion in the plot at low frequencies and far downstream locations. A fairly clear difference in coherence exists between regions where

the FS is a dominant contributor and regions where the LS dominates. At $z < 8$ m, where FS noise is greater than LS noise, the coherence is significantly lower than elsewhere, except at frequencies and positions where BBSAN is present in the spectrum (from 600-800 Hz for $z < 4$ m for 75% ETR and from 350-700 Hz for $z < 6$ m for 150% ETR). Consistent with results of Tam *et al.* [1], downstream locations, where Neilsen *et al.* [17] identify LS noise as the dominant contributor, the coherence is significantly elevated. Neilsen *et al.* also identify FS noise as being present at the locations farthest downstream at 150% ETR, aft of the maximum radiation region, but not at the frequencies shown in this figure.

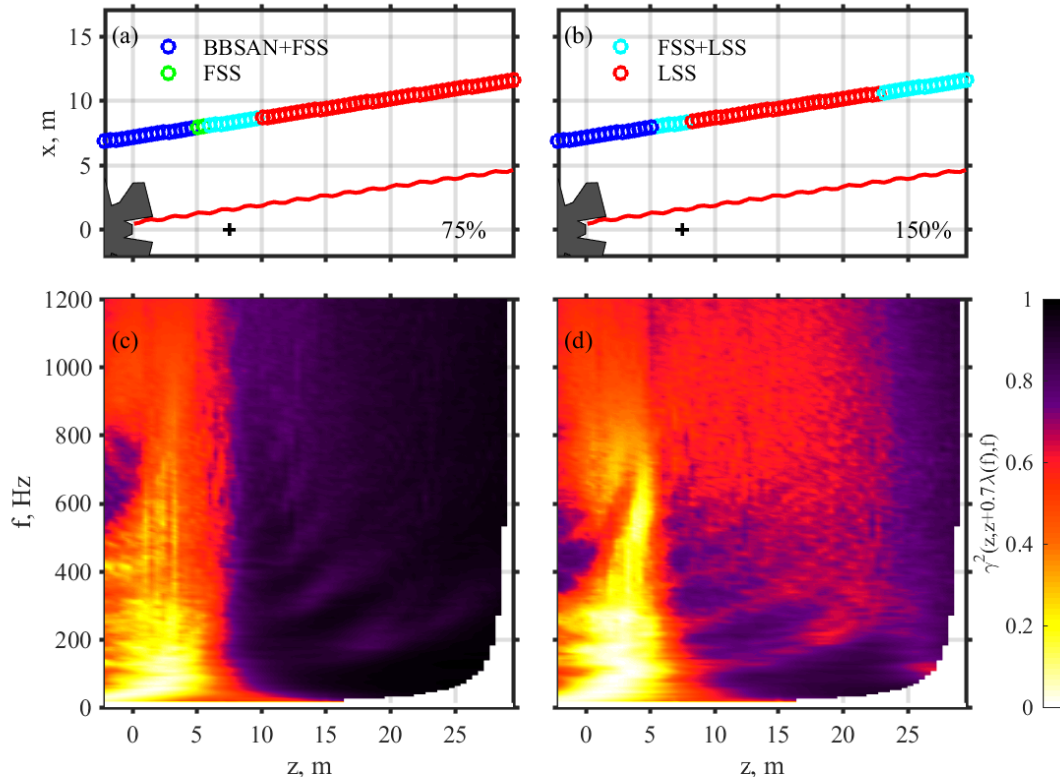


Fig. 9 (a,b) Schematic of the dominant noise sources in each portion of the overall field as determined in the spectral analysis of Neilsen *et al.* [17] for 75% ETR and 150% ETR. (c, d) Local coherence between points at z and those at $z + 0.7\lambda(f)$ downstream from the reference location (Eq. `refeq:coherenceNonDInput`) for 75% and 150% ETR, respectively. In parts (a) and (b), the assumed peak source location is marked as a +, the nozzle is marked using a triangle, and the approximate shear layer is represented as a wavy red line.

The local coherence in Fig. 9 is generally greater for 75% ETR than 150% ETR, which is consistent with the (broadband) peak cross-correlation coefficients in Fig. 8. The LS-dominated spatial region for 150% ETR has significantly greater levels, but with significantly lower local coherence. While both LS and FS components typically grow in level with increased engine power, the LS noise increases more rapidly. Because noise radiates efficiently from LS turbulence structures only for portions of the wavenumber spectrum with supersonic phase velocity, increasing the jet velocity is expected to increase the relative sound yield from the LS mechanism inasmuch as larger portions of the wavenumber spectrum become supersonic [1]. Jet conditions including the convective Mach number are not publicly available for this military nozzle; however, one would in general expect an increase in velocity with increased engine power and an associated increase in the relative prominence of the LS noise production mechanism over FS noise production; however, this is not uniformly true. In the spectral decomposition of Neilsen *et al.* [17], the peak measurable levels of the two sources differ by only about 7 dB for 150% ETR while they appear to vary by around 9 dB at 75% ETR. Thus, this phenomenon of greater coherence at lower engine power seems more uniform than can be easily explained solely by an increase in FS relative to LS. If increased levels were the only issue, one would expect the variation in coherence to follow the balance of spectral contributions from the FSS and LSS spectral shapes, but this is not observed. Also notable in Fig. 8 is the presence of a set of lobe structures visible as darkened regions of higher coherence with less

coherent regions in between. This phenomenon as well as its potential role in reducing coherence are discussed in Sec. IV.B. Whatever the ultimate cause, the decrease in coherence with increased engine power is likely to result in increased complexity of modeling at higher engine power conditions if, for example, a wave packet-type source [11], is employed. Whatever the cause, the peak radiation region is less coherent at higher engine power conditions, a fact corroborated by similar results in the peak cross-correlation coefficient of Fig 8 shown previously.

4. Coherence length

Harker *et al.* [16] calculated coherence lengths in the upstream direction (Fig. 12 of Ref. [16]). For the sake of comparison, the F-35B upstream coherence lengths, $L_{\gamma^2}(z, f)$, using Eq. 6, are shown in Fig. 10, with the vertical axis showing frequency on a log scale. Grayed-out areas show positions where the array was not long enough to place an upper bound on $L_{\gamma^2}(z, f)$ at that frequency. Harker *et al.* [16] noted that the FS noise contributions were associated with shorter coherence lengths and LS noise was associated with longer coherence lengths. Consequently, coherence lengths at lower frequencies in the downstream direction were significantly longer than those in the sideline or upstream directions. These observations appear to agree with the F-35B results as there is a decrease in coherence length (Fig. 10) in approximately the regions where FS noise contributions were identified by Neilsen *et al.* [17]: approximately $z < 10$ m in the 75% ETR case and about 8 m in the 150% ETR case. Harker *et al.* also note particularly low values in the coherence lengths in regions where the FS and LS overlap. Consistent with their observation, the lowest coherence values appear to occur between about $z = 5 - 7$ m in Fig. 10, in the midst of the FS+LS noise overlap region identified by Neilsen *et al.* [17].

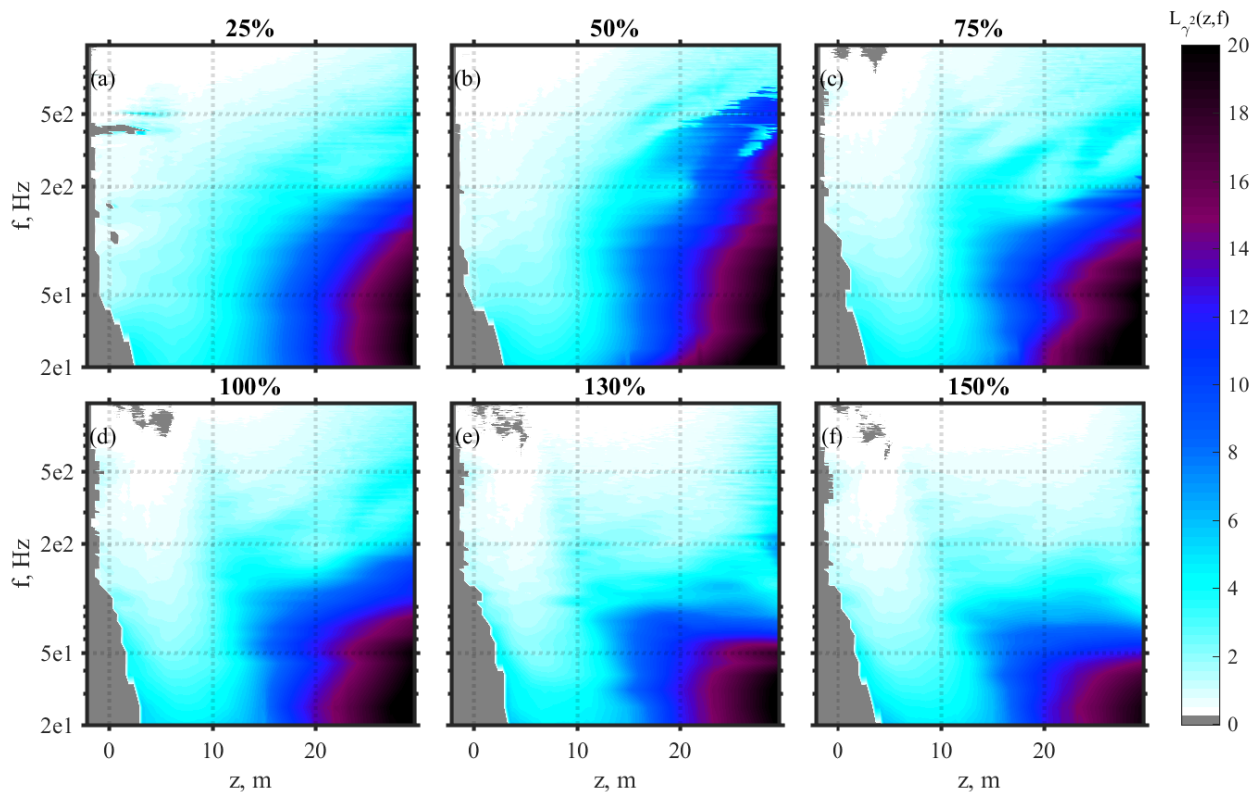


Fig. 10 $L_{\gamma^2}(f, z)$, upstream coherence length as a function of frequency, f , and downstream distance, z , for engine power conditions of (a) 25%, (b) 50%, (c) 75%, (d) 100%, (e) 130% and (f) 150% ETR. Areas where the array was not sufficiently long to resolve the maximum coherence length are grayed out.

Harker *et al.* [16] used coherence lengths to show that a contraction in coherence occurs with increased engine power. They noted that the high coherence lengths associated with the downstream, LS-dominated region extended to much higher frequencies at an intermediate engine power condition than at maximum afterburner. With our more detailed set of engine power conditions, we can, in addition to confirming their observation of the general trend, state that the

decrease in coherence with increased engine power takes place, for the most part, gradually. The highest frequency exhibiting relatively large coherence length at aftward LS-dominated locations decreases slightly with each incremental increase in engine power. One possible exception is that the coherence may decrease more rapidly or slowly due to the spatial positioning of the relatively more coherent spatospectral lobes. Overall, however, the sound field is gradually becoming less coherent and more energetic in the maximum radiation direction as engine power increases. This finding strengthens the prior similar observations of Harker *et al.*

B. Multiple Spatospectral Lobes

1. Motivation and background

Perhaps the most striking feature visible in the spatial variation of the spectra in Fig. 2 is the presence of multiple spatospectral lobes, which account for at least the top 3 dB of the highest amplitude noise emitted by the jet. The significance of this phenomenon can be seen by simply evaluating the maximum level across the array as a function of frequency as in Fig. 11(a) for 150% ETR. Multiple peak frequencies are evident, with a difference of at least 3 dB at intermediate frequencies. To further quantify the impact of the spatospectral lobes on received levels, the narrowband autospectral density levels are considered on a continuous line through space and frequency (as shown in Fig. 11(b)) passing through the approximate centers of the spatospectral peaks. The levels along this white line are plotted in Fig. 11(c); the difference between levels at and between the spatospectral lobes can be as great as 4 dB. Three conclusions are possible from this observation: 1) the spatospectral lobe production mechanism is the source of the most prominent set of components in the sound field of this aircraft, 2) this phenomenon is in some way able to modulate or redistribute energy across frequency and position both increasing and decreasing levels, or 3) whatever led to the intervening nulls between the spatospectral lobes is among the more effective sound suppression mechanisms demonstrated for full-scale jet noise. In any case, the spatospectral lobe phenomenon in jet noise from high-performance, tactical aircraft engines is significant and needs to be better understood in the interest and pursuit of effective noise reduction solutions.

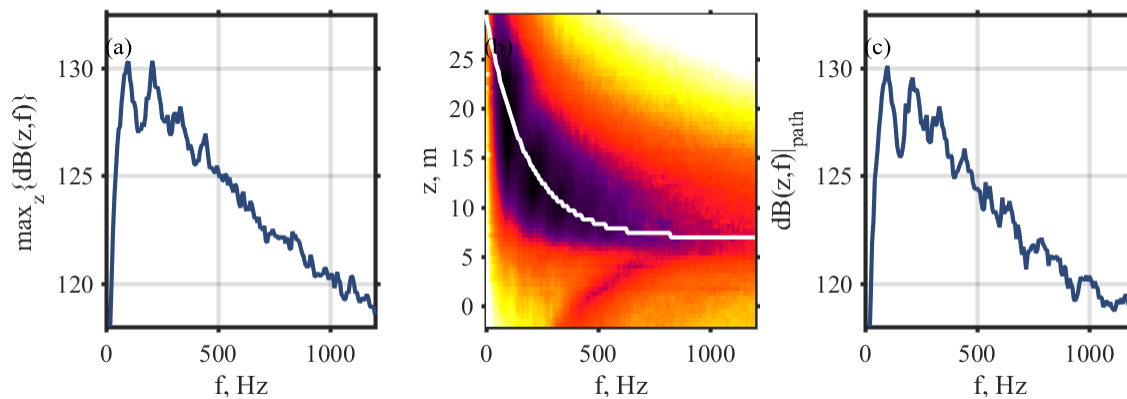


Fig. 11 (a) Maximum spectral level (dB re $20 \mu Pa / \sqrt{Hz}$) at 150% ETR across array locations at each frequency. (b) Spatospectral map of autospectral density levels (dB re $20 \mu Pa / \sqrt{Hz}$) with a white contour that passes through the approximate locations of the spatospectral lobe peaks. (c) Spectral levels evaluated along the white contour showing the variation in levels due to the spatospectral lobes.

In the past several years, the study of spatospectral lobes in jet noise has increased. First identified by Wall *et al.* [41] in measurements of a rectangular-nozzle high performance tactical aircraft, the multiple spatospectral lobe phenomenon has subsequently been examined using multisource statistically optimized near-field acoustical holography (M-SONAH) by Wall *et al.* [29, 31, 42], and by Leete *et al.* [43]. Tam and Parish [44] have suggested that the presence of the second lobe in the one-third-octave spectra of Neilsen *et al.* [35] (who analyzed the same tactical aircraft as Harker *et al.* [16]) could be attributed to indirect combustion noise. Wall *et al.* [29] and Leete *et al.* [43], on the other hand, suggested that the presence of multiple spatospectral lobes might be related in some way to the shock cell interactions, citing evidence from Liu *et al.* [6] regarding numerical studies and Long [45] regarding the use of NAH on a lab jet to indicate that the source region was striated. The mechanism or mechanisms responsible for the multiple spatospectral

lobes have not been conclusively determined.

2. Spectra

In the present study, the multiple spatio-spectral lobe phenomenon becomes clearly visible in the spectra of Fig. 2 beginning at 50% ETR, where they appear as dark slanted regions indicative of higher levels. By 50% ETR some clear divisions are apparent; however, the lobes are tilted in frequency (with lobe peak frequency increasing at positions farther downstream). At higher engine power conditions, lobe peak frequency increases less with downstream array position. At 75% ETR, when the BBSAN appears, five lobes are clearly visible with a possible, partially formed, sixth. This is also the case for the higher engine power conditions. The number of lobes seen in this study is significantly greater than that seen in the prior full-scale study of Harker *et al.* [16] and the prior F-35 studies of Wall *et al.* [29, 31, 41] in which this phenomenon was identified. These features tend to be more easily discerned when the narrowband frequency is plotted linearly (as is the case here) rather than in the more conventional logarithmic presentation of frequency. The lobes tend to congregate spatially in the peak-frequency region with the higher frequency lobes tending to be the closest to the center of the peak in OASPL. Additionally, the lowest frequency lobe appears to be responsible for the upward bend in OASPL seen at around 23 m in engine conditions of 50% ETR and above.

As engine power condition increases, the spatio-spectral lobes of Fig. 2 move upstream and become more localized in frequency and space. Looking, for example, at the 50% ETR condition of part Fig. 2(e), the main lobe (the lowest-frequency lobe farthest downstream) stretches from around $z = 12.5$ m to beyond the length of the array while for 150% ETR (l), the main lobe begins around $z = 11$ m and ends around $z = 29$ m. At 50% ETR, the main lobe also extends to higher frequencies near 275-300 Hz than at 150% ETR, where the main lobe is below 200 Hz. Similar observations can be made about the second lobe (second dense black region from the bottom) at 50% and 150% ETR: this lobe stretches from about $z = 9.5 - 22$ m to at 50% ETR and approximately $z = 8.5 - 19$ m at 150% ETR. It is not immediately clear why increased engine power condition leads to increased frequency locality of the lobes. The upstream movement of the lobes may be related in some way to changes in convective Mach number, a pattern present generally with LS/Mach wave-type noise sources. Because only the top 20 dB of the sound field are visible in Fig. 2, the apparent increase in locality is probably best interpreted as increased peakedness of the spectrum at lobe locations and frequencies rather than a decrease in levels elsewhere. Nevertheless, the effect is a narrowing of the lobes in frequency, at least relative to their peak narrowband levels.

Additionally, for 150% ETR, the peak frequencies of the lobes are approximately 100 Hz, 206 Hz, 319 Hz and 444 Hz—remarkably close to approximating a harmonic series. A polynomial approximation to the frequencies of the spatio-spectral peaks of $f_c = 4.75 + 90.75n + 4.75n^2$ provides a very close approximation. Wall *et al.*'s [31] have suggested that the multiple lobe phenomenon may be related to the location of shock cells in the jet plume, and this may also account for the peak frequencies of the lobes as well as perhaps their positioning, though this requires further study.

The approximate spatial positions of the peaks on the array at 150% ETR are $z = 22.5, 15, 12.5, 10$ and 8 m, which would make their locations appear to approach the same limiting downstream distance as the MARP. The spatio-spectral locations of the lobes warrant further investigation to determine which behavior patterns are consistent across different full-scale jets and which are merely idiosyncratic. At higher frequencies, the highest spatio-spectral lobes and the BBSAN occupy the same portion of the array as can be seen in Fig. 2, particularly for (j), (k) and (l).

3. Correlograms

Single-reference correlograms provide additional insights into the multiple spatio-spectral lobe phenomenon. In this section, the envelope $A(\tau)$ of the cross-correlation is plotted on a logarithmic scale for convenience in considering signals at differing levels and is referred to as a correlogram. The downstream position is represented on the horizontal axis and the correlation time delay at each microphone is shown on the vertical axis; the amplitude of the absolute value of the correlation envelope is represented using the color map. By examining the time delay-position slope of correlated components—seen as streaks in the correlograms—one can determine the phase speed (the speed with which a phase surface of the component is traversing the array) and with it the direction of travel of sound components. One can also determine the relative strength of sound components traveling in differing directions or with differing phase speeds.

Examination of the correlograms shows that noise components exhibiting differing phase speeds and thus different far-field directionality are present within the sound field. While some of these are likely due to differences between lobes, others appear to be due to structure within a lobe. In Fig. 12, a set of correlograms for all six engine conditions is shown for a reference microphone located at $z = 11.45$ m). This reference location was chosen because multiple spatio-spectral lobes have large values at this location.

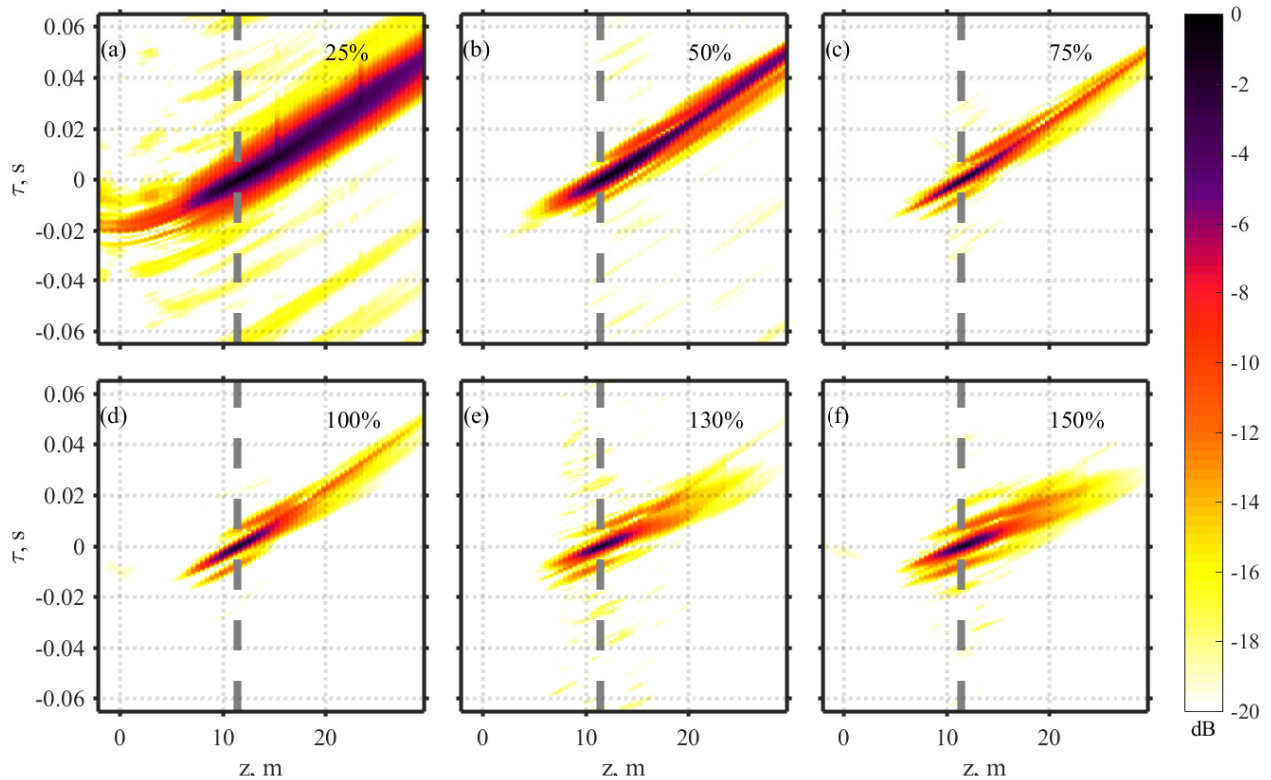


Fig. 12 Cross-correlograms for all engine conditions referenced to microphone at $z = 11.45$ m.

At this midfield position, correlated sound components with at least two slopes (and thus directions of travel) appear in the correlograms. The prominence of the two appears to shift with increasing engine power and the slope of one of the two components (but not the other) appears to change with engine power. This can be seen by comparing the plots for 75% and 150% ETR. At 75% ETR (c), the main, thin correlative streak begins at the reference location and zero delay, and proceeds, from there, up and to the right until reaching approximately $\tau = 0.05$ ms at the farthest downstream array position. This thin component decreases in relative magnitude as engine power increases, though it is still barely visible at 150% ETR as a light yellow line. Also as engine power increases, a second component gradually separates from this line and assumes a shallower slope, becoming more prominent and more shallow with increasing engine power. At 150% ETR (f), this second component is significantly more prominent. This streak begins from the same point, but follows a much lower slope until about $\tau = 0.03$ ms. The original streak appears to maintain its phase speed regardless of changes in ETR, resulting in a constant directionality. The slope of the second component, however, appears to be decreasing corresponding to the angular direction of travel of this component moving away from the jet plume toward the sideline at higher engine powers. For a further detailed analysis of the changes in F-35B spatio-spectral lobe propagation directions across frequencies and engine conditions calculated using holography methods, see Ref. [43].

The differing phase speeds across the microphone array can also be seen farther downstream, where overall correlation is greater. A bifurcated correlation pattern was seen by Harker *et al.* [16] at their highest engine condition and a location far downstream. Similar to their results, the clearest example of explicit bifurcation of the correlation pattern is seen when the last microphone ($z = 29.54$ m), is used as reference, as shown in Fig. 13. From 50% to 150% ETR, the region of high correlation at the reference microphone, as well as elsewhere, appears to thicken significantly. This may be explained by appeal to the spectra of Fig. 2, which show a wider band of prominent frequencies arriving at the last microphone at lower engine powers than the comparatively narrower low-frequency band at the highest engine powers. A signal that is narrower in frequency exhibits more ringing in its autocorrelation, which results in thickening in time of the correlation envelope. Examining another feature of Fig. 13, a slight separation is seen in the slopes within the main correlative streak at engine power conditions as low as 50% ETR: Multiple streaks clearly meet at the reference microphone location following different slopes for $\tau < 0$. The different slopes correspond to different phase speeds and produce different delays across the array beginning around $z = 6 - 7$ m. The bifurcation is slight at 75% ETR and increases a bit at 100% ETR. At 130% and 150% ETR, the separation between sets of streaks is clear. At 150% ETR

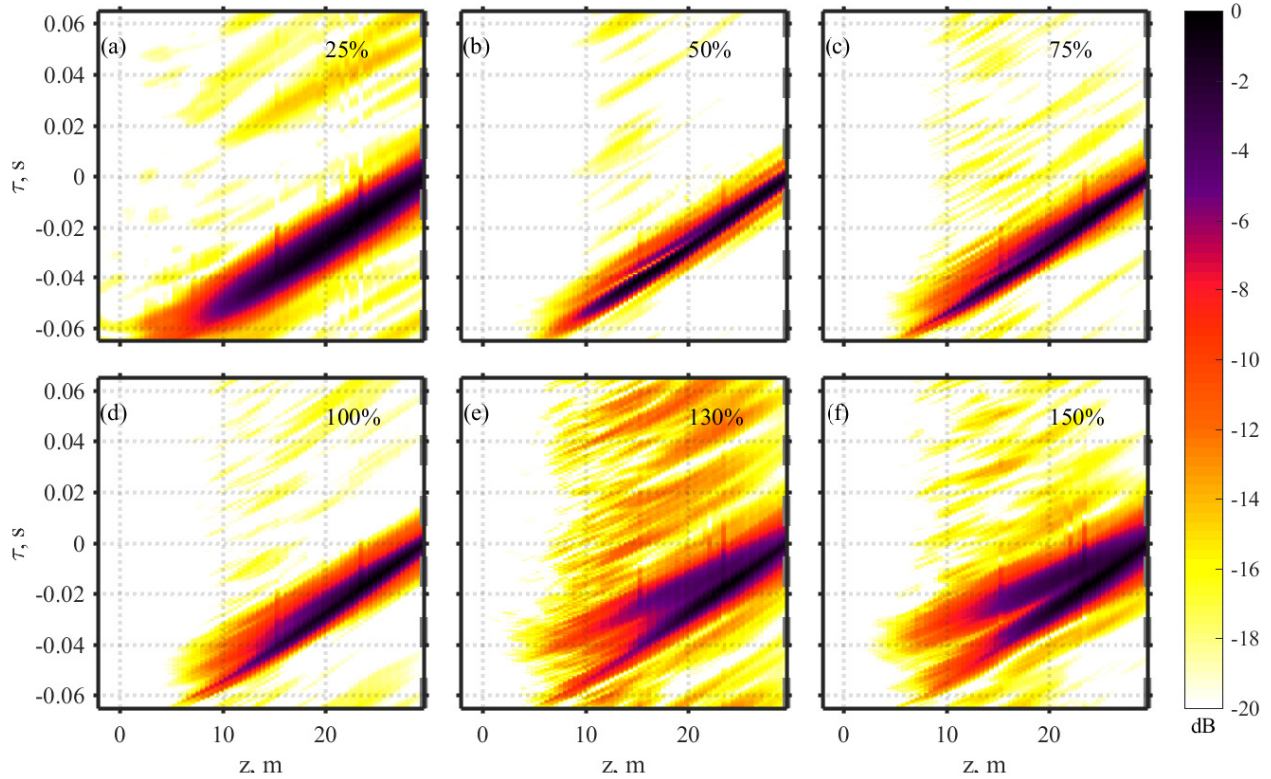


Fig. 13 Correlograms of A in decibels for all engine conditions referenced to microphone at $z = 29.54$ m.

there appear to be two main groups of streaks, one ending at about ($z = 5$ m, $\tau = -0.04$ s) and the other ending at about ($z = 7$ m, $\tau = -0.055$ s). Each of these groups of streaks appears to be comprised of at least two sub streaks. This latter observation suggests that there is more structure to the correlative streaks, and thus to the underlying phenomenon producing them, than has heretofore been appreciated.

When the reference microphone location is at the downstream end of the array, the noise is dominated by the first spatio-spectral lobe. Thus, the substantial split in the delay slope (phase speed and thus direction of propagation) is initially unexpected. In order to evaluate the significance of the bifurcated correlative streaks seen in Fig. 13 with regard to the far-field propagation direction, the slope of the two branches of the streak is used to determine approximate directions of arrival at the array. The relative straightness of the streak suggests that the radiation arriving at the array is effectively plane wave-like or conical wave-like, such that a clear hyperbolic turning point is not visible. Thus, planar or conical phase surfaces are assumed for the propagation. The direction of travel for such a wave is perpendicular to the phase surfaces, the two forming a right angle. The acute angle that the direction of travel forms with the line array is θ . This acute angle is then one corner of a right triangle, with the hypotenuse being the effective phase speed along the array c_{eff} and the adjacent leg being the speed of sound c . The noise causing a correlative streak in the correlogram originates from an angle, with respect to the line array, of

$$\theta = \cos^{-1} \left(\frac{c}{c_{\text{eff}}} \right). \quad (9)$$

By picking points on the correlogram for 150% ETR, the resultant phase speeds and propagation angles are estimated for the two main streaks and listed in Table 1.

Upon calculating the angles relative to the engine inlet, θ_{inlet} , associated with these phase speeds, the directions of travel are 117.5° and 155° (see Fig. 1). Given the feathering that is present at the end of the 150% ETR (MAXAB) correlogram (i.e., two main streaks appear to separate further into sub-streaks) with reference at $z = 29.1$ m, one could envision dividing the main correlative streaks into further sub-streaks and determining effective phase speeds and directions of arrival for these as well. However, it is not clear whether these are the results of distinct but noisy differences in direction of travel or continuous but noisy ranges of direction of travel. While the sub-streaks may provide

Table 1 Points on a 150% ETR (MAX AB) correlogram and the phase speeds along the array of the associated streaks in.

Point	z	Δz	τ	c_{eff}	θ	θ_{inlet}
Ref	29.54 m	0 m	0 s	N/A	N/A	N/A
1	14.61 m	14.93 m	0.02555 s	584.3 m/s	54.0°	117.5°
2	17.78 m	11.76 m	0.03285 s	358.0 m/s	16.5°	155.0°

a fruitful question for further study, for the purposes of this paper, it seems sufficient to point out that the broadband sound arriving at the end of the array is traveling in groups moving in two very distinct directions. The change in the θ_{inlet} for the two main branches of the bifurcated correlative streak likely account for the shift in far-field directivity seen in James *et al.* [30] with increased engine power condition and thus help explain the phenomena observed in the far field. Future analyses should consider examining bandpass-filtered correlograms in order to separate the several components present in these signals or, alternatively, determine individual component directivity from the array cross-spectral phase. This might also enable the positive identification of the particular frequency components involved in each portion of the bifurcated directivity pattern.

4. Single-reference coherence

Notwithstanding the potential utility of those future analyses, the frequency components leading to the bifurcation can be investigated via the single-reference coherence plots in Fig. 5 in Sec. III.C. In part (f) of this figure, the reference microphone is the same location as used in the correlogram (Fig. 13), and a split in the region of large coherence is visible, which is visually similar to that seen in the correlogram. However, in this case the vertical axis and, consequently, the split, is in frequency. The upward trend and particular frequencies at which the split occurs are of interest: The split runs between from approximately 70 to 120 Hz over $z \approx 8 - 25$ m. Careful examination of Fig. 2(l) reveals a similar split in lobe 1, indicative of a barely visible spectral manifestation of the more complicated structure indicated by the propagation directions of the bifurcation in the correlogram. Further, the upper branch of the split in the single-reference coherence plot (Fig. 5(f)) seems to exhibit some of the same sort of separation of the upper branch into sub-branches that is seen in the correlation. However, given the available resolution of this plot, this observation serves more as an interesting possibility for further exploration than as a conclusive statement of a significant phenomenon. A similar large split in the coherence at far downstream locations was seen in the full-scale study of Harker *et al.* However, because their spectral data was presented in one-third-octave bands, it is not presently possible to verify whether a split in the spectra similar to ours was present in their study. Future theories that attempt to describe these phenomena will hopefully consider these fine structural features as well as the more obvious aspects of the lobe pattern.

5. Single-frequency array coherence

Insights into the relationships between lobes can be gained from evaluation of the array coherence at frequencies where multiple spatio-spectral lobes are present. This follows the approach taken in the prior full-scale study of Harker *et al.* [16], in which reduced coherence between lobes was seen for noise from a nominally rectangular-nozzle, high-performance jet engine (e.g., see Fig. 13 of Ref. [16]). For the F-35B, the same features are evident in the single-frequency array coherence and narrowband levels at 137.5 Hz for an engine power condition of 100% ETR, as shown in Fig. 14. Because array geometry effects somewhat obscure the visible contraction of the neck in the array coherence when viewed solely in linear coordinates, the array coherence is shown as a function of both z (left) and angle (right). In both cases, a significant neck, or narrowing of the region of high coherence, is visible at the same locations at which the dip in the narrowband level marks the boundary between two competing lobes. The position of the dip in level is marked with a gray line in all plots for a visual reference. The peaks are also marked with black or white lines to allow more precise comparisons between the level and coherence patterns. The dip in the narrowband level accords precisely with the narrowing of the coherence. The point at which the coherence is minimal occurs when each lobe contributes approximately equally to the sound field because then they are in matched competition. The peaks in level are not aligned with the peaks in coherence probably for related reasons. Because the lobes are both contributing, the narrowband level peaks are a superposition of the two producing a combined peak OASPL closer to the interface between the lobes than if the lobes could be measured individually. Because the lobes are mutually

incoherent, interference between the lobes causes the peak of the coherence to occur farther away from the interface than if each were measured individually. Thus, the peak coherence and the peak level associated with a pair of mutually incoherent lobes are displaced from the individual lobe centers by some amount in opposite directions as we see here.

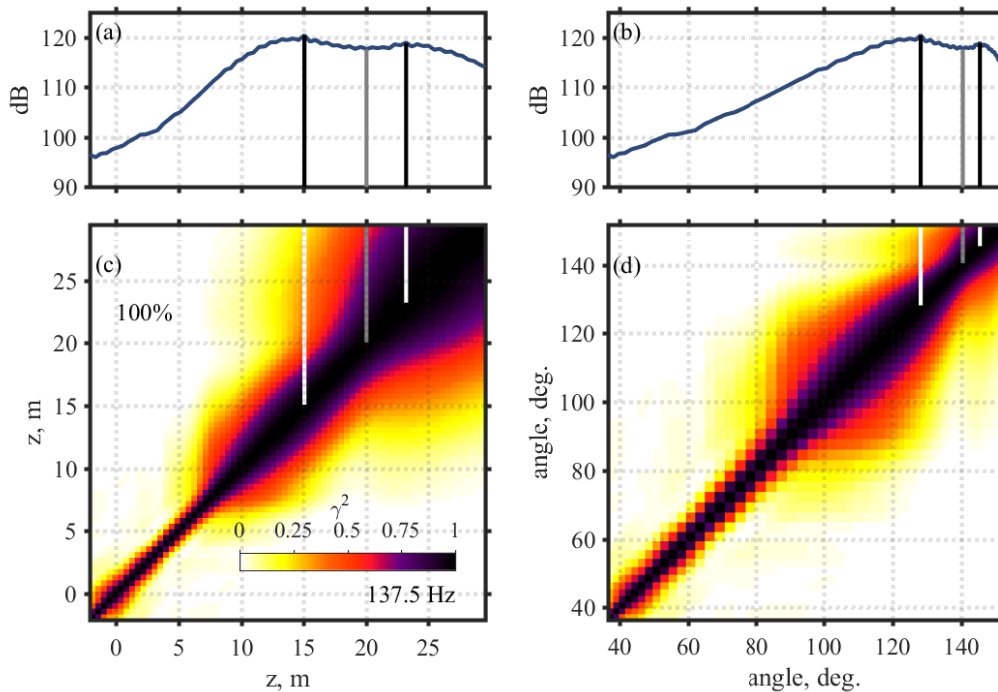


Fig. 14 (a,b) Narrowband autospectral density levels (dB re $20 \mu\text{Pa}/\sqrt{Hz}$) and (c,d) array coherence for $f = 137.5 \text{ Hz}$ at 100% ETR shown as a function of z (left) and angle (right). Note the presence of a dip in the narrowband level between the lobes around $z = 19 \text{ m}$ in (a) and 138° in (b) and the corresponding neck shown in the two coherence maps below, (c) and (d), respectively. The location of this dip is marked by a gray line in each case. The location of the OASPL peaks are marked by black or white lines.

In confirming the results of Harker *et al.*, the present study suggests that the coherence of the multiple spatio-spectral lobe phenomena appear to be insensitive to the difference of nozzle geometry between the two full-scale jets. The fact that the lobes are incoherent with one another also confirms that they are not just delayed or scattered versions of the same radiation phenomenon but exhibit a degree of independence.

6. Coherence length/summary coherence

Because the coherence differs between spatial regions where spatio-spectral lobes compete and where one lobe appears to dominate, summary measures of coherence ought to be effective tools to map the positions of the spatio-spectral lobes. However, a brief examination of Fig. 10, which shows upstream coherence length, $L_\gamma^2(z, f)$, as a function of position (horizontal coordinate) as a function of frequency (vertical coordinate) fails to confirm this expectation. Although traces of lobes can be detected in this plot, $L_\gamma^2(z, f)$ in its dimensional form favors lower frequencies with their associated longer wavelengths. Lower frequency $L_\gamma^2(z, f)$ values are artificially inflated to such an extent that the effect dominates and thus hides much of the more subtle lobe structure. Some success in visualizing the coherence structure of the lobes was realized in Fig. 9 (Sec. IV.A) where the local coherence a nondimensionalized distance from each reference position was shown, though the color contrast in that case was not ideal for this application.

When, instead, the coherence lengths in Fig. 10 are nondimensionalized by the wavelength (Eq. 7), as seen in Fig. 15, a more direct comparison across frequencies is enabled. Here, the linear frequency axis employed (instead of the logarithmic one used in Fig. 10) enables direct comparisons between the spectral and coherence characteristics of the lobes. As a consequence of the nondimensional presentation of coherence lengths, $L_\gamma^2(z, f)/\lambda(f)$, the presence of

self-coherent and mutually incoherent spatospectral lobes becomes easily apparent. At the center of each lobe, a region of high coherence is present and at each interface a region of lessened coherence is present. The phenomenon is most visible at 75% ETR because the increase in frequency with downstream position of the lobes allows for good contrast at that engine power condition. However, visually comparing the plots for other power conditions, some portion of the phenomenon appears to be visible at all engine states. At 50% ETR, the $L_\gamma^2(z, f)/\lambda(f)$ pattern matches the orientation and locations of the first four identifiable lobe features. Even at 25% ETR, some lower frequency $L_\gamma^2(z, f)/\lambda(f)$ features shared with the higher engine power conditions appear to be present, such as the tooth-shaped feature (darker blue in the plot) aft of 10 m and below 600 Hz, though the differences in noise sources present in this case result in a fruitless search for type of higher-frequency lobe features present at higher engine power conditions. The small angular aperture covered by microphones at the end of the array lead to increases in coherence length toward the end of the array.

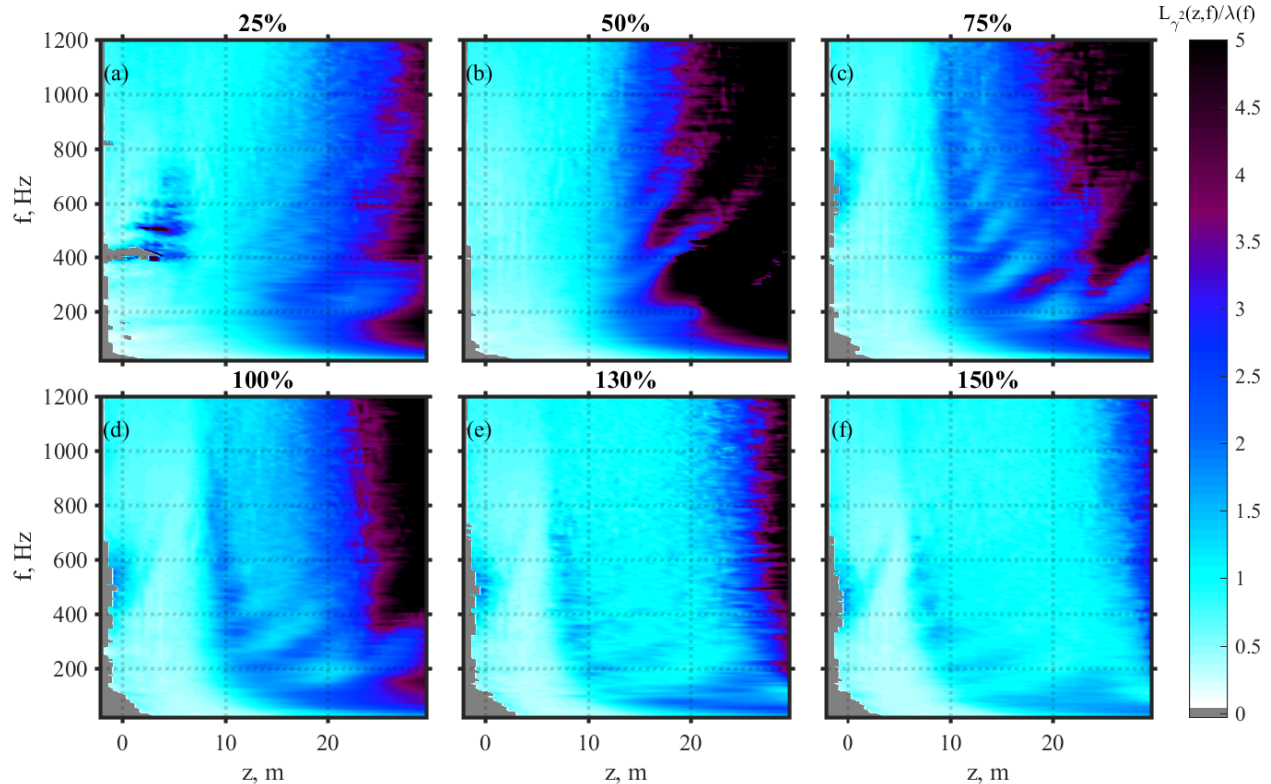


Fig. 15 $L_\gamma^2(f, z)/\lambda(f)$, upstream coherence length nondimensionalized by wavelength, λ , as a function of frequency, f , and distance downstream, z , for engine power conditions of (a) 25%, (b) 50%, (c) 75%, (d) 100%, (e) 130% and (f) 150% ETR. Areas where the array was not sufficiently long to resolve the upstream coherence length are grayed out.

With comparisons across frequency thus simplified, it is apparent that lower frequencies and higher frequencies display nondimensionalized coherence lengths more comparable than was previously clear, i.e., they are coherent over comparable numbers of wavelengths.

All regions of expected LS-domination based on the spectral identifications of FSS and LSS of Nielsen *et al.* [17] for 75% and 150% ETR show some increase in coherence length over FS-dominated regions. Although spectral identifications were only available for 75% and 150% ETR, similar noise types may be inferred at similar positions between and adjacent to these engine conditions. The similarities in coherence length patterns support this view. Additionally, both LS and FS noise-dominated regions appear to have decreased coherence length for increased engine power. The decrease in coherence in FS-dominated regions may be attributable to a broadening of the FS source location, as this would increase the variety of directions from which FS could arrive at the array. There is also a noticeable effect of ETR on the location at which coherence lengths begin to rise visibly in Fig. 15. The increases in the nondimensionalized coherence length in the LS-dominated region appear farther upstream as engine power increases, consistent with the expectation that noise from large-scale turbulence structures radiates farther from the jet axis as jet

velocity increases. However, similar changes occur in variation in coherence specifically associated with the lobes. A forward shift in larger coherence lengths is seen for the higher frequency lobes—supporting spectral evidence that their directivity shifts forward as engine power increases. Lower frequency lobes appear to change position relatively less as assessed spectrally and precise changes are difficult to evaluate in coherence because the overall coherence is decreasing with increasing engine power. Nevertheless, the spatio-spectral lobes appear to demonstrate similar directivity behavior to the Mach wave radiation mechanism, implying that they are perhaps a manifestation of the same phenomenon or a closely related one.

When using nondimensional coherence length, it is again clear (as discussed in Sec. IV.A) that coherence length decreases as engine power condition increases. Looking across engine conditions from 50% to 150% ETR, the coherence length associated with the lobes decreases roughly uniformly across frequency with each increment in engine condition. Each of these conditions, nevertheless, allows a visible distinction between the less coherent region associated with FS noise and the more coherent region associated with LS noise, as may be observed by comparing the forward and aft positions, respectively. Part of this reduction in coherence appears to be attributable to the behavior of the lobes themselves: The lobes are mutually incoherent. There is some indication that the decreases in coherence due to the interference between spatio-spectral lobes may be cumulative and result in a field which is less coherent overall. The degree of overlap and, thus, interference appears to be directly related to the engine power condition. It was noted in Sec. IV.B.2 (during the discussion of spectra) that the spatio-spectral lobes become less inclined (increase less) in frequency with increased downstream measurement position as engine power condition increases. Thus, the lobes appear to become flatter in frequency. If each lobe is still of similar real spectral width to its counterparts at differing engine conditions, then the amount of overlap between the lobes must increase as the frequency/position slope decreases, as it does with increased engine power. Consider, for example, Fig. 16, which shows spectra (left) and nondimensionalized coherence lengths (right) for 75% (top) and 150% ETR (bottom) conditions. The lobes in the spectra at 75%, part (a), are better separated leading to strong coherent lobes in part (b). At 150% the spectral lobes, part (c), are flatter and closer together with greater degree of overlap, leading to less coherence within the lobes seen in part (d).

The nondimensionalized coherence lengths suggests that the global decrease in coherence seen in the field is directly attributable to the change in frequency/position slope of the spatio-spectral lobes and that this phenomenon is then the primary driver of coherence variability that must be accounted for in modeling the full-scale jet noise field. This phenomenon may also explain decreases in sound field orderliness with ETR noted above in the dimensional coherence length and peak cross-correlation (see Sec. IV.A). While balances between LS and FS noise contributions may also play a role, lobe overlap appears to be an additional important factor in the reduction of the coherence associated with spatio-spectral lobes as engine power increases.

7. Discussion of Spatio-spectral Lobes

In coming to terms with the possible causes of the multiple spatio-spectral lobe phenomenon, it is worthwhile to discuss some of the possibilities that can be excluded. In a previous study by Swift *et al.* [46], it was shown that the autocorrelation did not contain any peaks sufficiently prominent to indicate multipath interference in the multilobe region. The correlogram results also preclude scattering because scattering sources produce a distinct pattern on a cross-correlogram. Thus, the correlogram suggests (and the coherence agrees) that the same acoustical information is not being received at a simple delay in the multilobe region but that each lobe is associated with a coherent source, which is largely incoherent with other similar sources. This somewhat limits the possible mechanisms that can be proposed as explanations. The number of lobes seen along the ground array near the F-35B also excludes theories that are not able to account for the plurality of lobes produced by this phenomenon: as many as six. The change in the spatial directivity of the lobes with engine condition suggests that they may be sensitive to convective Mach number. The arrangement of lobes with lower frequencies directed further downstream than higher frequencies also may suggest an origin related to differing positions in the plume in which different length scales of turbulence mature. Theories to explain some or all of these results might include the presence of multiple convective Mach numbers and associated families of Mach waves and their differing directivities [22, 23], or an origin in turbulence/shock interactions of some sort as suggested by Wall *et al.* [29] might explain the spatial arrangement of lobes. Whether these successfully account in whole or in part for this phenomenon remains uncertain. There is also some evidence linking the multilobe phenomenon with phenomena related to BBSAN, as addressed in the next section.

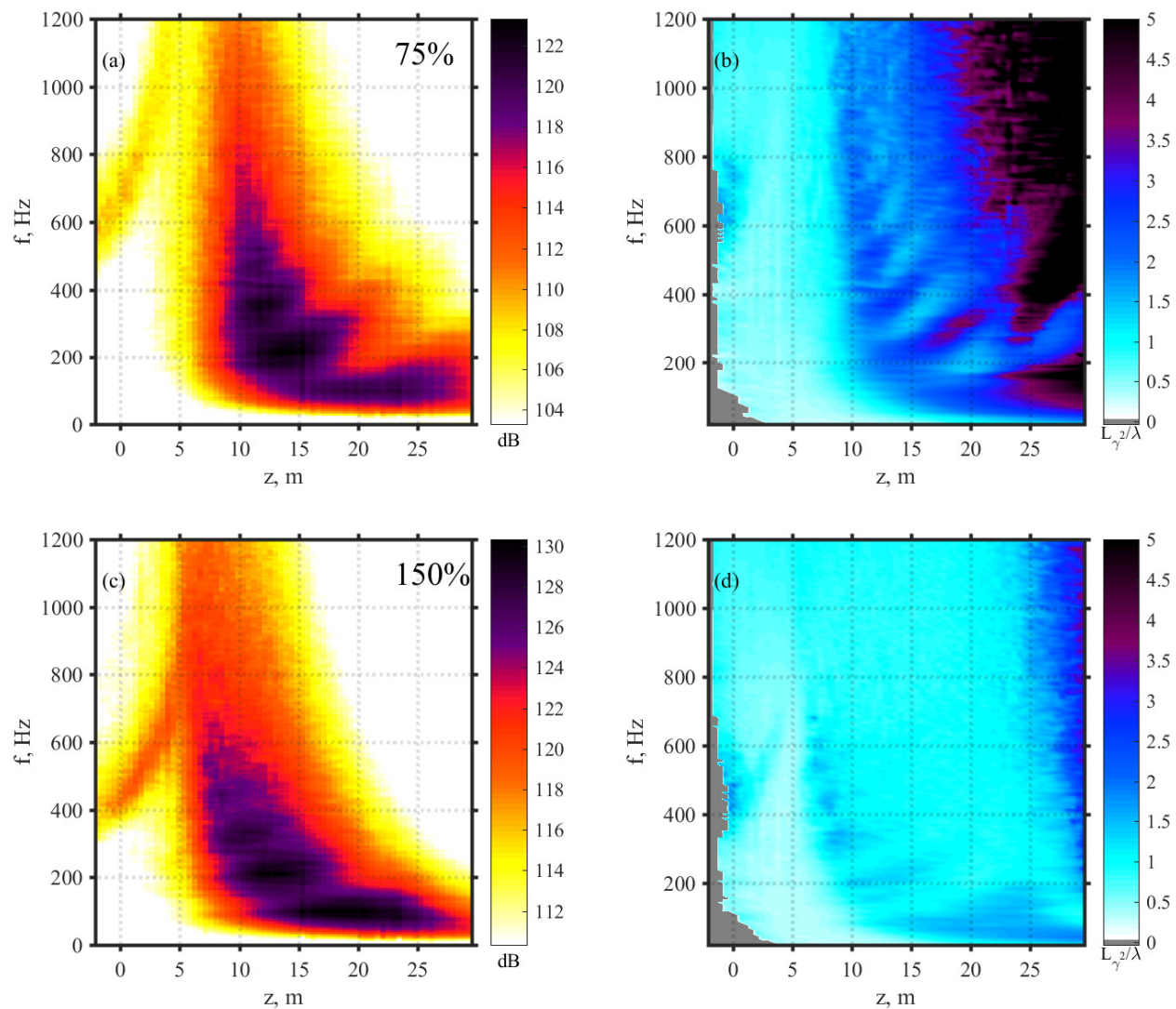


Fig. 16 (a) Autospectral density levels (dB re $20 \mu\text{Pa}/\sqrt{Hz}$) and (b) $L_\gamma^2(f, z)/\lambda(f)$, upstream coherence length nondimensionalized by wavelength, λ , as a function of frequency, f , and distance downstream of the nozzle, z , for engine power conditions of 75% (top) and 150% (bottom) ETR.

C. Broadband Shock-Associated Noise

1. Background

Broadband shock-associated noise results from the interactions of large-scale turbulent structures with the shock cells present in imperfectly expanded, supersonic jets. The start of serious efforts to describe and model BBSAN is often dated to the model of Harper-Bourne and Fisher [47] and Tanna's [18] subsequent use and experimental investigation of that model's validity. Further model development was undertaken by Tam *et al.* [37, 38, 48] and, later, Kuo *et al.* [19, 20]. This work focused on laboratory-scale jets, and the applicability of lab-scale models to full-scale jets is a topic of active investigation. Tam [49] recently presented one-third-octave band data that suggest some differences in behavior may exist in BBSAN between laboratory and full-scale jets, and Neilsen *et al.* [17] have provided a three-way spectral decomposition of the F-35B noise measurements under study here into FS and LS noise and BBSAN components. A spatiotemporal characterization of BBSAN in full-scale jets is thus of significant interest.

2. Spectra

BBSAN is evident in the F-35B noise field (Fig. 2) for roughly $z < 5\text{ m}$ and makes significant contributions at 75% ETR and above. The BBSAN spectral peak is visible as a yellow and red-orange tail decreasing in frequency as z decreases from a downstream/high frequency limit at 1000 Hz around $z = 5\text{ m}$. The highest visible frequency in the BBSAN streak varies some as a function of engine power with higher engine powers associated with lower highest visible frequencies. The F-35 BBSAN peak frequencies vs. location and ETR are presented in Vaughn *et al.* [50], which also shows the variation in the level and width of the BBSAN spectral peak.

The level of the BBSAN signature increases with engine condition. The maximum narrowband BBSAN level at the array is around 108 dB for 75% ETR, 114 dB for 100% ETR, 117 dB for 130% ETR and just less than 120 dB for 150% ETR. Comparisons of BBSAN in the F-35B with laboratory scale studies of BBSAN for level and peak frequency across engine condition are complicated by potential changes in the geometry of the variable area military nozzles. Changes in engine condition could reasonably affect the area, strength and positions of shocks, as well as jet temperature, velocity and Mach number. Engine power condition may thus influence BBSAN levels through multiple intermediate variables complicating comparisons with more controlled laboratory settings.

Additional spectral features of the F-35B BBSAN are discussed in Neilsen *et al.* [17]. They applied a three-way spectral decomposition using the LSS, FSS and BBSAN spectral shapes and, in the process, found the peak frequency and OASPL associated with the BBSAN spectral contribution. They found a peak frequency for the BBSAN that appeared to linearly increase in log frequency with angle at 75% ETR and 150% ETR (MAXAB) at inlet angles (from the MARP) between 35° and 70° , the entire range over which it could be identified [17]. These shifts in the peak frequency of BBSAN as a function of angle have been previously addressed by theories ranging from a Doppler shift-related phenomenon [18] to Tam *et al.*'s [38] wavy-wall analogy.

3. Correlograms

Single-reference cross-correlation can provide fairly direct evidence of BBSAN. As was discussed previously, Fig. 3 shows correlation (a) and coherence (b) between adjacent pairs of microphones at several locations along the microphone array. The cross-correlation coefficient $r(\tau)$ shows clear ringing at the position farthest upstream, which is dominated by BBSAN—a characteristic of BBSAN as identified in Refs. [9, 16].

More interesting features are visible, however, when correlograms of the correlation envelope, A , across the entire array with a position of interest is considered. In Fig. 17, the correlograms for all six engine conditions references to the microphone farthest upstream ($z = -2.1\text{ m}$). The downstream position is represented on the horizontal axis and the correlation time delay at each microphone is shown on the vertical axis; the amplitude of the absolute value of the correlation envelope is represented using the color map. As is the case for the spectra in Fig. 2, Fig. 17 contains a fairly clear BBSAN signature, most easily detected in the upstream direction at engine power settings of 75% and above. The lack of similar signatures at 25% and 50% is consistent with the lack of observable BBSAN in the associated spectra. The BBSAN signature in the correlogram is visible from the reference position on the far left of the array to around $z = 2 - 3\text{ m}$, as expected. However, a puzzling feature appears in these correlograms: a second region of large correlation referenced to the microphone at $z = -2.1\text{ m}$ occurs around $z = 7.5 - 12.5\text{ m}$ —the maximum radiation region dominated by LS noise. In between these two regions of high correlation there is a reduction in correlation in the region dominated by FS noise [17]. The downstream region of high correlation with the BBSAN is unusual for several reasons: First, this second part of the BBSAN correlation signature is most visible in the middle of the spatio-spectral lobes of

the maximum radiation region, exactly where it should be least visible due to competition. Second, in this second region some portion of the noise is correlated with the BBSAN that is not evident in between the two correlated regions, where both the LS and FS noise are present. Furthermore, the BBSAN correlation signature appears at locations where BBSAN cannot be detected in the spectrum ($z = 7.5 - 12.5$ m) but not in the where it can be identified spectrally (around $z = 4 - 6$ m). Finally, the BBSAN signature is visible in the maximum radiation region but not visible farther downstream. These peculiarities raise the question as to how the high correlation around $z = 7.5 - 12.5$ m can be associated with BBSAN evident at $z = -2.1$ m.

The high correlation around $z = 7.5 - 12.5$ m referenced to $z = -2.1$ m suggests (at the least) that some component related to BBSAN is appearing at unexpected locations. Wider evidence on the subject may support the existence of situations in which BBSAN is detectable at angles farther aft. Kuo [20], for example, mentions the presence of BBSAN at aft locations during forward flight. BBSAN is also allowed to be present downstream in some models [18, 47], however, these models generally assume BBSAN is present everywhere, leaving open the question of why the signature is not more prominent in the correlogram in the region around $z = 4 - 5$ m. The measured correlation of the downstream signals with the BBSAN signature could indicate either a dual directivity to the BBSAN or, perhaps, information carried by the large-scale turbulence structures that are both actuating the BBSAN and supplying the same information as LS or Mach wave noise in the maximum radiation region. Whatever the cause, information associated with BBSAN is received at the farthest upstream location and the maximum radiation region.

The correlation time delay is slightly positive at the downstream location for 75% but decreases until the signature arrives at both points on the array simultaneously at 150% ETR. As engine power condition increases from 75% to 150% ETR, the disconnected correlated region appears to shrink in space, thicken in time, and move upstream. In two of these aspects, moving upstream and shrinking in space, the downstream correlated region matches the behavior of the spatio-spectral lobes in Fig. 2. Specifically, the position of the downstream correlated region appears to follow the position of the higher frequency spatio-spectral lobes in Fig. 2 at the peak frequency of the BBSAN at $z = -2.1$ m. In other words, if one were to trace the BBSAN spectra to its peak frequency at the forward end of the array and then follow that frequency across for increasing z , the location of the intersected lobe tends to match the region of increased correlation in the correlogram, Fig. 17. Reciprocally, the correlogram for a reference microphone in the midst of the spatio-spectral lobe region (e.g., $z = 10.1$ m at 150% ETR), shows high correlation with the BBSAN signature detected from the beginning of the array to 3.3 m downstream (or farther if a lower limit is employed on the correlograms). The measurable correlation between the BBSAN signature and the lobe locations appears to lend support to the proposition of Wall *et al.* [31] that the multiple spatio-spectral lobes result from shock cell interactions.

Returning to Fig. 17, additional features of the correlograms referenced to $z = -2.1$ m are of interest. First, the second correlated region is clearly broader in time than the first. While some ringing due to the narrowband nature of the BBSAN-related signature is expected, this ringing would apply to both locations and so seems an incomplete explanation. The broadening could be consistent with multiple copies of information (similar to that at the upstream location) arriving at the downstream position at regular delays with decreasing correlation for the flanking copies. Another oddity is that the slopes between the two sides do not appear to have the same magnitude. Finally, the lack of a clear turning point in BBSAN signature in these plots also requires some explanation. If sound is proceeding from a simple source with a stable location, then one would expect the resulting relative streak in the correlogram to form a vertex near the point on the array perpendicular to the source location, i.e., the point of closest approach. This vertex is expected as part of the hyperbolic trace produced by a static source in a correlogram. The lack of a vertex may be reflective of multiple shock-cell sound sources believed to participate in BBSAN generation. It may also be possible that FS noise is effectively masking the correlation in the middle region, though it is again unclear why it would not then be able to better mask the BBSAN correlation at a more distant downstream location dominated by LS in the maximum radiation region where FS noise is expected to contribute more. The lack of a vertex, and perhaps the differing slope magnitudes, suggests either an unusual pattern to the directivity of the BBSAN or the same information being broadcast by the BBSAN also being made available in the LS noise. The common origin of perturbation by the large-scale turbulent structures may lead the BBSAN and the LS noise to exhibit a degree of correlation not previously documented. Whatever the cause, the signals are detectably correlated at upstream and downstream locations but not at intermediate locations.

4. Single-reference coherence

The BBSAN and the related downstream signature evident in the correlograms may also be interrogated by examining frequency-dependent, single-reference coherence across the array. Indeed, additional interesting features of the signature

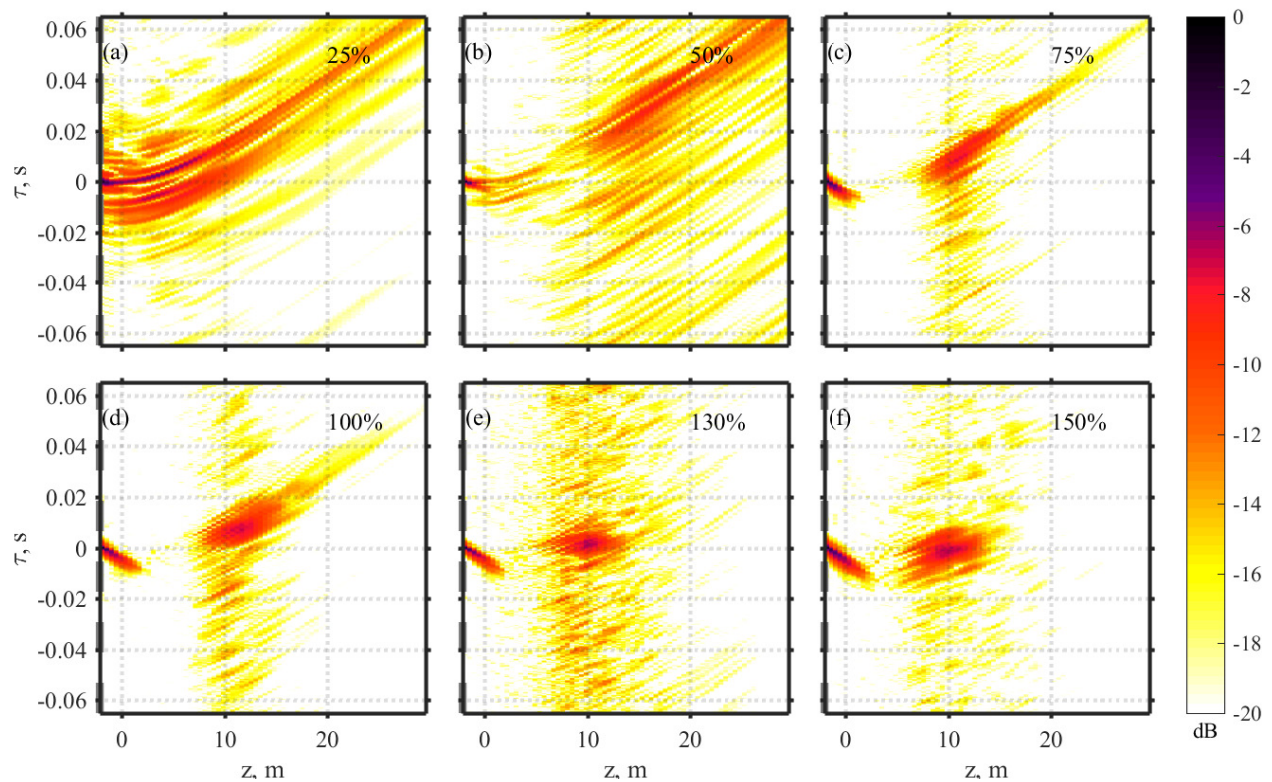


Fig. 17 Cross-correlograms for all engine conditions referenced to microphone at $z = -2.1$ m.

can be effectively visualized by comparing coherence for reference microphones at $z = -2.1, 2.9, 7.4$ and 11.5 m for 150% ETR (Fig. 18). In each case, a main region of high coherence exists around the reference location. Each also exhibits additional regions of coherence believed to be related to the BBSAN signature (indicated by black ovals). Beginning with the reference at $z = -2.1$ m (a), a downstream region of increased coherence is seen similar to the increased correlation for this same reference position. This separated coherent region includes frequencies about 300–425 Hz, roughly consistent with the frequency range BBSAN at $z = -2.1$ m, and covers $z \approx 6 - 13$ m, similar to the position of the forepart of the third lobe in Fig. 2. The coherence references to this first microphone location, thus, verifies the frequency connection between the spatio-spectral lobes and the BBSAN surmised from the correlograms. As z of the reference location increases (not shown), the separated region of coherence increases in frequency tracking the frequency of the BBSAN at the reference. When the reference is located further downstream in the spatial region covered by multiple spatio-spectral lobes, e.g., $z = 7.4$ m as in Fig. 18(c), a relatively continuous streak of coherence associated with the BBSAN is seen at the same frequencies as in the spectra of Fig 2(l). That the BBSAN should become visible at the same position as that covered by the multilobes is consistent with their sharing acoustic information. If the reference is placed farther aft, beyond the spatial span of the higher frequency lobes as in Fig. 18(d), then higher frequency portion of the BBSAN coherence signature disappears. That reference placement outside of the lobe structure for a given frequency should result in loss of coherence with the BBSAN signature is consistent with information sharing between the lobes and the BBSAN signature. Taken together these single-reference coherence plots seem supportive of a theory connecting the lobe structures with the downstream presence of information related to the BBSAN signature. However, Fig. 18(b) complicates this picture. The circled feature in Part (b) looks similar to the BBSAN signature of part (c), except that it is downstream of the reference location of $z = 2.9$ m and has opposite frequency/position slope trends as if it were mirrored. The features in both (b) and (c) appear to tend toward a similar spatial location at higher frequencies. The combination of this set of features, thus, raises the possibility that the correct explanation for the correlation and coherence between the BBSAN and noise farther downstream may be multifaceted: It may be the case both that the spatio-spectral lobes share information with the BBSAN and that BBSAN is radiated to the maximum radiation region, though this idea requires further investigation. The single-reference coherence is a

profitable way to examine both possibilities.

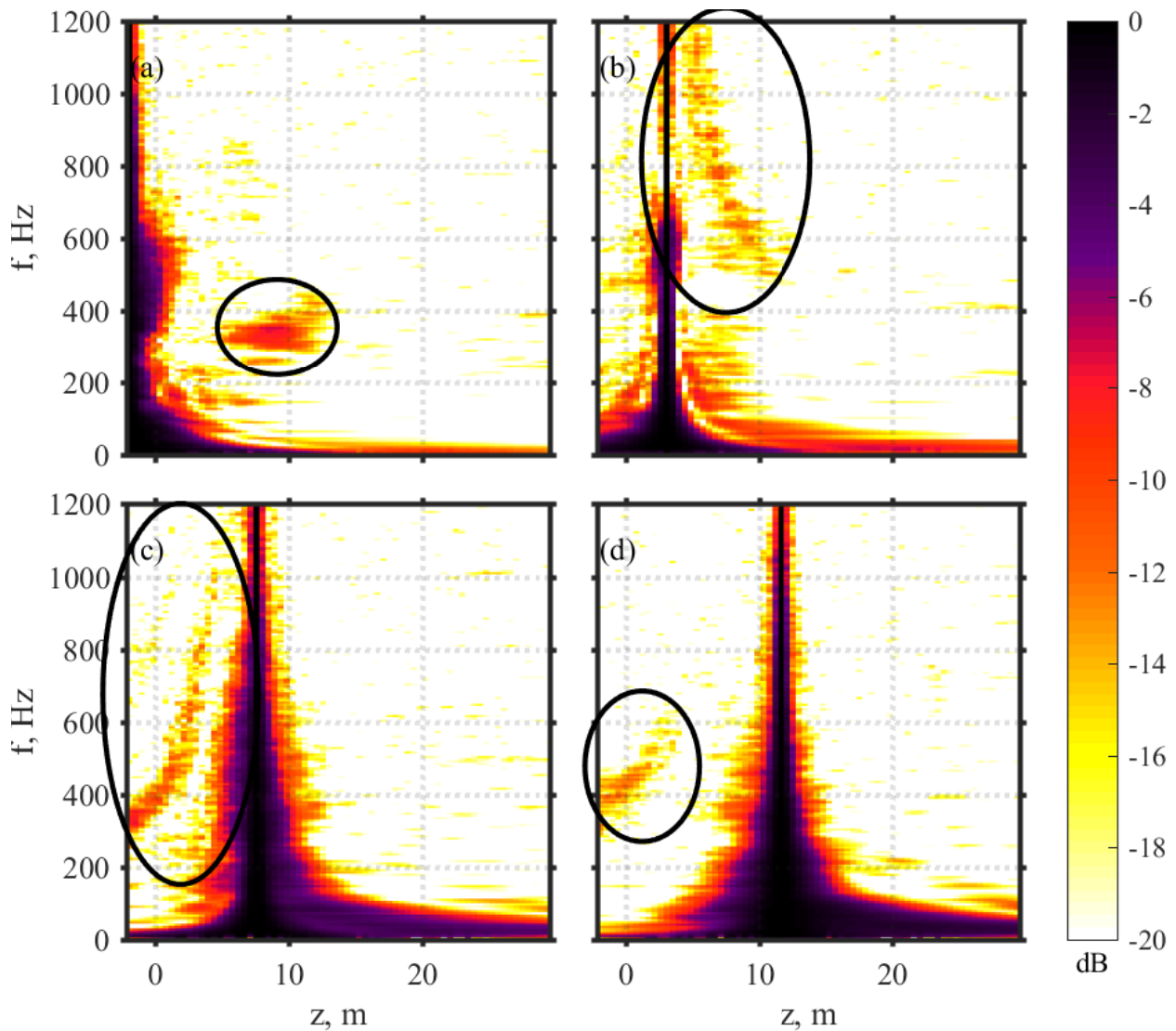


Fig. 18 Single reference coherence plots for four reference microphone locations with BBSAN-relevant features: $z = -2.1, 2.9, 7.4$ and 11.5 m. Ovals indicate features of interest in each plot.

5. Summary measures of coherence

Because the BBSAN production mechanism results in a coherent signature in the field, the summary coherence measures tend to be elevated at places and frequencies impacted by BBSAN. This is visible in Fig. 15 in Sec. IV.B, which shows upstream coherence lengths that are slightly increased at the farthest upstream positions at the frequencies of the BBSAN signatures that can be identified in the spectra of Fig. 2 at corresponding engine conditions. The increased coherence values for the BBSAN are also visible in Fig. 9, which shows the coherence evaluated at a point 0.7 wavelengths downstream of each microphone location. The visibility is also improved in that figure because the downstream rather than the upstream look direction was used. If the downstream direction is used, then the coherence is typically evaluatable at all upstream locations, while if the upstream coherence length is used, the coherence is typically evaluatable at all downstream locations. The summary measures of coherence, thus indicate, an increase in field coherence of the BBSAN spectral peak relative to the FS noise.

V. Conclusion

Spatio-temporal-spectral analyses have been used to evaluate the sound field received along a 71-microphone line array roughly parallel to the jet shear layer of the F-35B. Spatiospectral levels, correlation and coherence measures, as well as the summary coherence methods of coherence length and local coherence, have probed three phenomena of the noise field: turbulent mixing noise, multiple spatio-spectral lobes, and broadband shock-associated noise.

A. Mixing Noise

Relationships within the sound field have been examined to assess the presence of various types of turbulent mixing noise. Large-scale turbulent structure noise exhibits significantly greater coherence and correlation over longer distances than noise from fine-scale turbulence. Although the effects of these distinct sources are visible in simple slices of the correlation (Eq. 4) and coherence matrices (Eq. 5) and dimensional coherence length (Eq. 6, detectability is increased when measures of local coherence (Eq. 8) and nondimensionalized coherence length (Eq. 7) are employed. These local coherence measures have enabled enhanced comparisons across frequency and show clear boundaries in space and frequency for the contributions of the different noise sources. This study has confirmed that the coherence properties associated with large and fine-scale noise sources in prior laboratory-scale studies [1, 40] are similar at full-scale. The techniques used in this study point towards improved tools for future identification of these noise sources.

As engine power condition increases, the region of high field coherence moves forward. Mach wave radiation from large-scale turbulence structures produces high field coherence and the observed change in position of the high coherence region is consistent with the expected change in directivity in response to increased engine power. Information about the sound field from coherence measures was also compared with the spectral decomposition of the sound field of the present F-35B into LSS, FSS and BBSAN spectral components that was performed previously by Neilsen *et al.* [17]. The coherence information shown here confirms and corroborates the classifications in that work. Indeed, future spectral decomposition efforts could benefit from a merged spectrum and coherence-based approach to characterizing and classifying the noise from jets.

The sound field near the F-35B has also been compared with the full-scale, approximately rectangular-nozzle, tactical aircraft engine noise reported in Harker *et al.* [16]. Similar patterns of decreasing coherence with increasing engine power have been observed. In both jets, as engine power increases, the field becomes simultaneously more energetic and less coherent, posing challenges for modeling efforts. The present study, by using nondimensionalized coherence length, has further clarified that these decreases in coherence length with increased engine power are taking place across frequencies and positions in the typically LS noise-dominated regions. The decreases in coherence with engine power appear to be linked to the coherence properties of the multiple spatio-spectral lobes in the received sound field.

B. Multiple Spatio-spectral Lobes

The presence of multiple spatio-spectral lobes—regions where multiple significant peaks exist in maps of the spectral levels—is evident in the vicinity of the F-35. As many as 4-6 lobes are visible at engine conditions of 75% ETR and above, with evidence of 2 or more lobe structures present in both coherence and power spectra at 50%. These spectral peaks account for as much as a 4 dB increase in level over the spectra at intermediate positions and frequencies; if the multiple lobes are due to a distinct mechanism, they may be a dominant noise source for full-scale jets. The spatio-spectral lobes appear to decrease in frequency/position slope as engine power increases and also appear to contract spatially. The peaks of the higher-frequency lobes also appear to move upstream as engine power increases consistent with the typical changes in directivity of large-scale turbulent structure noise indicating, possibly, some dependence of the phenomenon on convective Mach number. The frequency arrangement of the lobes appears to be orderly but not precisely harmonic, with a polynomial providing a close approximation of the peak frequencies at 150% engine thrust request (ETR).

The spatio-spectral lobes appear to exhibit distinct directivities as determined using correlograms to characterize propagation phase speeds across the array. The direction of propagation of some spatio-spectral lobes changes as a function of engine power while others appear to be constant. The prominence of individual components of a given propagation direction also changes across engine conditions. A bifurcated correlated streak, indicative of components with starkly different directions of travel was noted when the farthest downstream position was used as the reference location of the correlogram, similar to that seen by Harker *et al.* [16]. This reference position, located spatially in the midst of the lowest-frequency lobe, suggests the lobe itself has a bifurcated structure. This was confirmed by examining the single-reference coherence, which showed a considerable split in the coherence of the lobe, a feature only barely

visible in the spectra. The sub-branches apparent in the correlogram and single-reference coherence indicate that the main lobe is itself more structurally complex than has heretofore been appreciated. This is consistent with results of Leete *et al.* [43] using holography, which show that apparently combined lobes in the near field may divide into separate lobes in the far field. Though there are aspects of these results that we do not yet understand, these results should be carefully considered in attempting to construct models that explain these phenomena.

Examination of coherence across the multiple lobes has shown that, similar to the findings of Harker *et al.*, the spatio-spectral lobes are self coherent but mutually incoherent, confirming that the lobes are not delayed or scattered versions of one another (a fact also confirmed by correlation analyses) but appear to provide self-coherent, mutually incoherent radiation arriving at the line array. Because the spatio-spectral lobes are self-coherent and mutually incoherent, summary measures of coherence and nondimensionalized coherence length are effective in identifying the lobe structure and can be favorably compared with the spectral structure of the lobes.

The simultaneous decrease with engine power in frequency/position slope of the spatio-spectral lobes and the mutual incoherence of the lobes appear to combine to drive global decreases in the coherence of the field associated with increased engine power. Thus the multiple spatio-spectral lobe phenomenon is both a peak noise phenomenon and a key complicating factor in efforts to model the noise from modern, tactical aircraft. The mechanism or mechanisms which combine to produce as many as six self-coherent but mutually incoherent spatio-spectral lobes of differing far-field directivity exhibiting as much as 4 dB of prominence over adjacent features in the F-35 requires further study and elucidation.

C. Broadband Shock-Associated Noise

Broadband shock-associated noise (BBSAN) is visible in the spectral patterns associated with F-35B engine power conditions of 75% ETR and above. The spectral level of the signature increases with increasing engine power. Higher engine power also produce lower peak BBSAN frequencies. More detailed analyses of frequency and level trends for this F-35 dataset may be found in Vaughn *et al.* [50] BBSAN contributes to elevated coherence, local coherence, and coherence length measures, in contrast to the fine-scale turbulent mixing noise found in adjacent regions and at neighboring frequencies.

Cross-correlation techniques have shown not only that a BBSAN-related signature is visible at the upstream locations typically expected for BBSAN, but also that noise in the maximum radiation direction also exhibits higher-than-expected correlation with the BBSAN. In between these two regions, the correlation is much lower. The correlation time delay between the two portions is slightly positive at the downstream location for 75% but decreases until the signature arrives at both points on the array simultaneously at 150% ETR. That BBSAN is correlated with noise in the peak radiation region is a surprise as this is typically the area in which it should encounter the strongest competition from the most prominent normal jet noise source, the LS or Mach wave radiation or, in this jet, the multiple spatio-spectral lobes. Instead, the coherence results have confirmed that a portion of the information present in the BBSAN peak at the first microphone position (serving as reference position) is present at downstream locations at the frequencies of the BBSAN peak. Peak cross-correlation results for the intersection of these two regions confirm that the amount of shared information between the upstream BBSAN and the downstream component is sufficiently large to be regarded as significant. Indeed the coherence information could reasonably be used in connection with the spectra to characterize the levels of this sound component at some future time. Single-reference coherence measures (across frequency and array position) show that a coherence feature consistent with the BBSAN signature appears at positions both upstream and downstream of different reference microphone positions suggesting, perhaps, a sort of rough symmetry in the behavior of the BBSAN. Single reference coherence also appears to show a significant relationship between the BBSAN and the multiple spatio-spectral lobes.

The mechanisms responsible for the BBSAN signature showing correlation and coherence with both upstream and downstream locations are currently uncertain; however, two possibilities seem worthy of further investigation. First, the BBSAN has a dual directivity that sends sound predominantly upstream and downstream with little (or band-limited) contribution at some intermediate angles. Second, the common presumed origin of the peak radiation region and the BBSAN is actuation by the large-scale turbulence structures and allows information contained in the large-scale structures to be imprinted upon both mechanisms so that it is manifested both at positions where the BBSAN and where the LS noise is present. A third possibility, based upon the suggestion of Wall *et al.* [31] is that a common origin of the multiple lobes and the BBSAN is shock interactions that, perhaps, serve as a point of departure for families of Mach waves and might mediate the sharing of information between the two regions. Though none of these can be conclusively proven at this point and more than one mechanism may contribute to the relationship, what we can conclusively state is

that correlation and coherence link the BBSAN signature with signals received in the maximum radiation direction and in midst of the spatio-spectral lobes.

D. Possible Links Between the Broadband Shock-Associated Noise and the Multiple Spatio-spectral Lobes

Prior authors, notably Wall *et al.* [29], have suggested the possibility that the multiple spatio-spectral lobe phenomenon was in some way related to interactions involving the shocks. In the midst of investigating both the spatio-spectral lobe phenomenon and the unusual features in the BBSAN-related signatures, some modest evidence has accumulated that may point to a relationship between the two phenomena. First, the same engine conditions that exhibit higher numbers (4-6) of spatio-spectral lobes coincide with the appearance of BBSAN. That the same engine conditions exhibit BBSAN and have similar spectral lobe structure patterns could indicate that they are linked by changes in the shock cells or turbulence characteristics in the vicinity of the shocks or other factors. Second, in the correlograms referenced to the farthest upstream microphone location, the downstream locations of the separated correlated region appear to match the locations of the spatio-spectral lobes at the frequency of the BBSAN at the reference microphone for that engine condition. This has currently only been verified for a limited set of position and requires further verification. Preliminary analyses with coherence also seems to support this result, but must ultimately be the subject of future work. Together, the correlation and coherence indicate a link between the spatio-spectral lobe features and the BBSAN and would be consistent with a multilobe etiology involving shocks.

In conclusion, spatio-temporal-spectral analyses of noise from the F-35B have sought to enable insight into both the sound field and its underlying causes by examining the relationships which exist in the resultant sound field. By examining such relationships, this paper has helped characterize important aspects of the sound field surrounding a high-performance military jet, helped compare and contrast the round-nozzle F-35B with the rectangular-nozzle jet aircraft of Harker *et al.* [16], and pointed out potentially important features of the sound field that have not been previously identified. These relationships ought to be explored and explained in order to increase understanding of the F-35B sound field, the aeroacoustics of heated, full-scale jets, and the broader category of jet noise as a whole.

Acknowledgments

The authors gratefully acknowledge funding for the measurements, provided through the F-35 Program Office and the Air Force Research Laboratory. (Distribution A: Approved for public release; distribution unlimited. F-35 PAO Cleared 5/16/2018; JSF18-529.) Analysis was supported in part through a grant from the Office of Naval Research Grant N000141410494 and an AFRL SBIR grant.

References

- [1] Tam, C. K., Viswanathan, K., Ahuja, K., and Panda, J., "The sources of jet noise: experimental evidence," *Journal of Fluid Mechanics*, Vol. 615, 2008, pp. 253–292.
- [2] Schlinker, R. H., "Supersonic jet noise experiments," Ph.D. thesis, University of Southern California, 1975.
- [3] Nance, D. K., "Separating contributions of small-scale turbulence, large-scale turbulence, and core noise from far-field exhaust noise measurements," Ph.D. thesis, Georgia Institute of Technology, 2007.
- [4] Panda, J., Seasholtz, R., and Elam, K., "Investigation of noise sources in high-speed jets via correlation measurements," *Journal of Fluid Mechanics*, Vol. 537, 2005, pp. 349–385.
- [5] Papamoschou, D., Morris, P. J., and McLaughlin, D. K., "Beamformed flow-acoustic correlations in high-speed jets," AIAA Paper 2009-3212, May 2009.
- [6] Liu, J., Corrigan, A., Kailasanath, K., Heeb, N., and Gutmark, E., "Numerical study of noise sources characteristics in an underexpanded jet flow," AIAA Paper 2014-2604, June 2014.
- [7] Baars, W. J., Tinney, C. E., Murray, N. E., Jansen, B. J., and Panickar, P., "The effect of heat on turbulent mixing noise in supersonic jets," AIAA Paper 2011-1029, January 2011.
- [8] Fuchs, H. V., "Space correlations of the fluctuating pressure in subsonic turbulent jets," *Journal of Sound and Vibration*, Vol. 23, No. 1, 1972, pp. 77–99.
- [9] Kumar, S. A., Karthikeyan, N., and Venkatakrishnan, L., "Correlation studies in the acoustic far-field of non-ideally expanded supersonic jets," AIAA Paper 2013-2082, May 2013.

- [10] Maestrello, L., "Two-point correlations of sound pressure in the far-field of a jet: experiment," *Journal of the Acoustical Society of America*, Vol. 59, No. S1, 1976, pp. S95–S95.
- [11] Harker, B. M., Gee, K. L., Neilsen, T. B., Wall, A. T., and James, M. M., "Beamforming-Based Wavepacket Model for Noise Environment Predictions of Tactical Aircraft," AIAA Paper 2017-4048, June 2017.
- [12] Fisher, M., Harper-Bourne, M., and Glegg, S., "Jet engine noise source location: The polar correlation technique," *Journal of Sound and Vibration*, Vol. 51, No. 1, 1977, pp. 23–54.
- [13] Viswanathan, K., Underbrink, J., and Brusniak, L., "Space-time correlation measurements in near fields of jets," *AIAA Journal*, Vol. 49, No. 8, 2011, pp. 1577–1599.
- [14] Jordan, P., and Colonius, T., "Wave packets and turbulent jet noise," *Annual Review of Fluid Mechanics*, Vol. 45, 2013, pp. 173–195.
- [15] Schlinker, R., Liljenberg, S., Polak, D., Post, K., Chipman, C., and Stern, A., "Supersonic jet noise source characteristics & propagation: Engine and model scale," AIAA Paper 2007-3623, May 2007.
- [16] Harker, B. M., Neilsen, T. B., Gee, K. L., Wall, A. T., and James, M. M., "Spatiotemporal-Correlation Analysis of Jet Noise from a High-Performance Military Aircraft," *AIAA Journal*, 2016.
- [17] Neilsen, T. B., B., V. A., Gee, K. L., Swift, S. H., Wall, A. T., Downing, J. M., and James, M. M., "Inclusion of Broadband Shock-Associated Noise in Spectral Decomposition of High-performance Military Aircraft Noise," AIAA Paper 2018-XXXX, June 2018.
- [18] Tanna, H., "An experimental study of jet noise part II: Shock associated noise," *Journal of Sound and Vibration*, Vol. 50, No. 3, 1977, pp. 429–444.
- [19] Kuo, C.-W., McLaughlin, D. K., and Morris, P. J., "Effects of supersonic jet conditions on broadband shock-associated noise," *AIAA Paper*, Vol. 2011-1032, 2011.
- [20] Kuo, C.-W., McLaughlin, D. K., Morris, P. J., and Viswanathan, K., "Effects of Jet Temperature on Broadband Shock-Associated Noise," *AIAA Journal*, Vol. 53, No. 6, 2015.
- [21] Liu, J., Corrigan, A. T., Kailasanath, K., and Gutmark, E. J., "Impact of chevrons on noise source characteristics in imperfectly expanded jet flows," AIAA Paper 2015-2835, June 2015.
- [22] Seiner, J. M., Ponton, M. K., Jansen, B. J., and Lagen, N. T., "The effects of temperature on supersonic jet noise emission," *14th DGLR/AIAA aeroacoustics conference*, Vol. 1, 1992, pp. 295–307.
- [23] Tam, C. K., and Hu, F. Q., "On the three families of instability waves of high-speed jets," *Journal of Fluid Mechanics*, Vol. 201, 1989, pp. 447–483.
- [24] Oertel, H., "Mach wave radiation of hot supersonic jets," *Mechanics of sound generation in flows*, 1979, pp. 275–281.
- [25] Oertel, H., "Mach wave radiation of hot supersonic jets investigated by means of a shock tube and new optical techniques," *Proceedings of the 12th International Symposium on Shock-Tubes and Waves, Israel*, 1980.
- [26] Oertel, H., "Coherent structures producing Mach waves inside and outside of the supersonic jet. Structure of complex Turbulent Shear Flow," *IUTAM Symp. Marseille*, 1982.
- [27] Greska, B., and Krothapalli, A., "On the far-field propagation of high-speed jet noise," *ASME 2008 Noise Control and Acoustics Division Conference*, American Society of Mechanical Engineers, 2008, pp. 129–133.
- [28] Gee, K. L., Sparrow, V. W., James, M. M., Downing, J. M., Hobbs, C. M., Gabrielson, T. B., and Atchley, A. A., "The role of nonlinear effects in the propagation of noise from high-power jet aircraft," *Journal of the Acoustical Society of America*, Vol. 123, No. 6, 2008, pp. 4082–4093.
- [29] Wall, A. T., Leete, K. M., Gee, K. L., Neilsen, T. B., James, M. M., and McKinley, R. L., "Preliminary Investigation of Multilobe Fighter Jet Noise Sources Using Acoustical Holography," AIAA Paper 2017-3520, June 2017.
- [30] James, M. M., Salton, A. R., Downing, J. M., Gee, K. L., Neilsen, T. B., Reichman, B. O., McKinley, R. L., Wall, A. T., and Gallagher, H. L., "Acoustic Emissions from F-35 Aircraft during Ground Run-Up," AIAA Paper 2015-2375, June 2015.

- [31] Wall, A. T., Gee, K. L., Neilsen, T. B., McKinley, R. L., and James, M. M., "Military jet noise source imaging using multisource statistically optimized near-field acoustical holography," *Journal of the Acoustical Society of America*, Vol. 139, No. 4, 2016, pp. 1938–1950.
- [32] Bendat, J. S., and Piersol, A. G., *Random data: analysis and measurement procedures*, John Wiley & Sons, 2011.
- [33] Harker, B. M., Gee, K. L., Neilsen, T. B., Wall, A. T., McInerny, S. A., and James, M. M., "On autocorrelation analysis of jet noise," *The Journal of the Acoustical Society of America*, Vol. 133, No. 6, 2013, pp. EL458–EL464.
- [34] Tam, C. K., Golebiowski, M., and Seiner, J., "On the two components of turbulent mixing noise from supersonic jets," AIAA Paper 1996-1716, May 1996.
- [35] Neilsen, T. B., Gee, K. L., Wall, A. T., and James, M. M., "Similarity spectra analysis of high-performance jet aircraft noise," *Journal of the Acoustical Society of America*, Vol. 133, No. 4, 2013, pp. 2116–2125.
- [36] Neilsen, T. B., Gee, K. L., and James, M. M., "Spectral characterization in the near and mid-field of military jet aircraft noise," AIAA Paper 2013-2191, May 2013.
- [37] Tam, C., "Stochastic model theory of broadband shock associated noise from supersonic jets," *Journal of Sound and Vibration*, Vol. 116, No. 2, 1987, pp. 265–302.
- [38] Tam, C., "Broadband shock-associated noise of moderately imperfectly expanded supersonic jets," *Journal of Sound and Vibration*, Vol. 140, No. 1, 1990, pp. 55–71.
- [39] Morris, P. J., "A note on noise generation by large scale turbulent structures in subsonic and supersonic jets," *International Journal of Aeroacoustics*, Vol. 8, No. 4, 2009, pp. 301–315.
- [40] Viswanathan, K., "Investigation of noise source mechanisms in subsonic jets," *AIAA Journal*, Vol. 46, No. 8, 2008, p. 2020.
- [41] Wall, A. T., Gee, K. L., James, M. M., Bradley, K. A., McInerny, S. A., and Neilsen, T. B., "Near-field noise measurements of a high-performance military jet aircraft," *Noise Control Engineering Journal*, Vol. 60, No. 4, 2012, pp. 421–434.
- [42] Wall, A. T., Gee, K. L., Neilsen, T. B., Krueger, D. W., and James, M. M., "Cylindrical acoustical holography applied to full-scale jet noise," *Journal of the Acoustical Society of America*, Vol. 136, No. 3, 2014, pp. 1120–1128.
- [43] Leete, K. M., Wall, A. T., Gee, K. L., Neilsen, T. B., and James, M. M., "Dependence of High-performance Military Aircraft Noise on Frequency and Engine Power," AIAA Paper 2018-XXXX, June 2018.
- [44] Tam, C. K., and Parrish, S. A., "Noise of high-performance aircraft at afterburner," *Journal of Sound and Vibration*, Vol. 352, 2015, pp. 103–128.
- [45] Long, D., "Jet noise source location via acoustic holography and shadowgraph imagery," AIAA Paper 2008-2888, May 2008.
- [46] Swift, S. H., Gee, K. L., Neilsen, T. B., Wall, A. T., Downing, M., and James, M. M., "Spatiotemporal analysis of high-performance military aircraft noise during ground run-up," *Journal of the Acoustical Society of America*, Vol. 142, No. 4, 2017, pp. 2512–2512.
- [47] Harper-Bourne, M., and Fisher, M., "The noise from shock waves in supersonic jets, AGARD CP 131," *Proc. of the AGARD Conference on Noise Mechanisms, Bruxelles, Belgium*, 1973.
- [48] Tam, C. K., and Tanna, H., "Shock associated noise of supersonic jets from convergent-divergent nozzles," *Journal of Sound and Vibration*, Vol. 81, No. 3, 1982, pp. 337–358.
- [49] Tam, C. K., Aubert, A. C., Spyropoulos, J. T., and Powers, R. W., "On the Dominant Noise Components of Tactical Aircraft: Laboratory to Full Scale," AIAA Paper 2017-3516, June 2017.
- [50] Vaughn, A. B., Neilsen, T. B., Gee, K. L., Wall, A. T., Downing, J. M., James, M. M., "Broadband shock-associated noise of a high-performance military aircraft," *Journal of the Acoustical Society of America – Express Letters*, (in preparation).